Superview-1 Remote Sensing for hydromorphological monitoring of shallow water streams within the Water Framework Directive

Thesis - Jitse Ruurd Nauta

07-07-2023
Student number: 7471092
First assessor: Dr. Menno Straatsma
Second assessor: Dr. Philip Kraaijenbrink
Program: MSc Applied Data Science, Utrecht University

ABSTRACT

Understanding change in river morphology is a crucial aspect to comprehend the complex and intertwined processes within a river ecosystem. The Dutch implementation of the Water Framework Directive (WFD) has established parameters that need to be monitored of river systems. One of those parameters included is hydromorphology. Although past studies emphasize the importance of measuring hydromorphology over time, this is not directly considered within this implementation of the WFD.

Beyond the WFD parameters, the objective of this study was to monitor the hydromorphology shallow streams on high temporal basis with Superview-1 images. The research goal was to assess which waterbody extraction method gained the highest accuracy based on the Superview-1 satellite images. The AHN lidar scans of the Netherlands were used as validation reference, as lidar sources are substantiated for their classification accuracy.

This research tested three waterbody extraction methods, including the Otsu threshold method, Supervised machine learning (Support Vector Machine) on a single training image, and Supervised machine learning (Support Vector Machine) on a multi-image training dataset. Accuracies for the threshold method, single-image SVM, and multi-image SVM were assessed to be 90% (Kappa: 0.70), 76% (Kappa: 0.50) and 90% (Kappa:072), respectively.

Going forward with hydromorphological monitoring of the shallow water streams, the Support vector machine trained on multiple images was used given its accuracy and kappa scores. By means of intersecting the extracted river polygons, with a pre-defined cross section, shift in riverbanks (left and right) and centre point was computed for an eroding and non-eroding section. This study revealed that a total shift of between 4.5 and 8.6 meters was recorded at the eroding section between the period of 2019 and 2023. At the non-eroding section, the shift remained between 0.2 and 1.3 meter between 2019 and 2023. A maximum shift of 13.1 meters was recorded at one of the cross sections at the right riverbank (eroding section).

This approach utilizing Superview-1 images has increased the temporal resolution of hydromorphology monitoring to approximately five yearly images. Towards monitoring the ecological status of shallow rivers, this research identified what the contribution of Superview-1 imagery could imply. Understanding trends in river (bank) shift at is crucial for creating context for monitoring ecological status, within WFD.

1 INTRODUCTION

Most of the water bodies in the Netherlands do not comply with the desired quality standards (CLO, 2022). These standards are defined in the Dutch implementation, "Kaderrichtlijn Water (KRW)", of the Water Framework Directive (WFD) set by the European Union(STOWA, 2020). The goal of the directive is to reach 'good' and non-deteriorating ecological status for all waterbodies in Europe (Kallis & Butler, 2001). Hydromorphology is one of the components in this directive. This parameter relevant for the shallow water streams in the Netherlands.

A review of literature reveals that temporal change in fluvial morphology is a key process to assess the health of a river ecosystem (Belletti et al., 2015; Corenblit et al., 2015; González del Tánago et al., 2021; Stutter et al., 2021). While change in fluvial morphology is not a parameter considered within hydromorphology from KRW perspective, Newson et al. (2006), Vogel et al. (2011), and Woodget et al. (2017) highlighted its importance due to the non-stationarity an uncertainty in hydrologic assessments. A key component in the definitions by these authors is that hydromorphology considers the change of the morphology of the river over time, whereas the KRW omitted the time component in their definition. This study goes beyond the definition of KRW and builds further upon the necessity of monitoring hydromorphology over time as substantiated within literature.

Monitoring of fluvial morphology - in terms of erosion, sediment transport, and deposition - ranged from, physical measuring, towards remote sensing (Table 1). Fundamental to these studies is that they rely on accurate measurements of the position of the studied waterbody. Earlier studies use manual measuring methods to extract the position of the waterbodies. Hooke (1979) used field measurements to monitor the river, newer studies of Winterbottom and Gilvear (2000), Large and Gilvear (2015), and Dragićević (2017)moved towards GIS approaches with airborne imagery. However, the authors still relied on manual delineation of the waterbody. Recent work of Langat et al. (2019) moved to automated waterbody extraction based on spaceborne remote sensing imagery.

Table 1,
Overview of existing research based on their study areas, findings, data type, and spatial and temporal resolution.

Authors	Data type	Study area (size)	Temporal resolution	Spatial resolution	Findings
(Hooke, 1979)	Field measurements	Devon, England	Study period of 2.5 years	n/a	Mean monthly erosion between 1 cm and 140 cm
(Winterbottom & Gilvear, 2000)	Aerial imagery	River Tummel (length of 6 km)	Four observations in 6 years	5m	Peak erosion of > 5 meters between images
(Large & Gilvear, 2015)	Google earth	Three rivers of different scales (between	Single assessment	n/a	n/a
(Dragićević et al., 2017)	Maps + Aerial photographs	Kolubara River basin (15 km section)	Seven observations in 87 years	n/a + 1m + 5cm	Bank erosion rate of 1.9 m year^{-1}
(Hemmelder et al., 2018)	UAV RGB	Petit Buëch river (0.4 km^2)	One observation per year	5cm/10cm	<20m channel displacement

(Langat et al., 2019)	Spaceborne RS Green + MIR	Tana River (length of 142 km)	Four observations in 42 years	30m	<980m channel displacement

Automated waterbody extraction on remote sensing images another well-studied area of research (Table 2). Recent reviews of the existing methodologies are performed (J. Li et al., 2022; Y. Li et al., 2022). J. Li (2022) stated five key methods for waterbody extraction to be single band threshold, multiband threshold (spectral index threshold), classification trees, machine learning models, object-oriented classification, and deep learning.

Table 2

Overview of existing research on the topic of waterbody extraction methods, comparing methods resolutions, and classification accuracy.

Authors	Type of method	Type of data	Included bands	Spatial Resolution (meters)	Classification accuracy (%)
(Donchyts et al., 2016)	CART + spectral indexes	Landsat 8 / SRTM	All Landsat bands	15, 30, 60 / 30	n/a
(Thanh Noi et al., 2017)	LULC – RF/KNN/SVM	Sentinel – 2	RGB[1] + 7 bands	20	90 – 95
(Mozgovoy et al.,2018)	Spectral index thresholding	Superview – 1	RGB + NIR[2]	0.50	82 – 90
(Langat et al., 2019)	Spectral index thresholding	Landsat Collection 1	RGB + MIR[3]	30	n/a
(Vos et al., 2019)	Deep learning + spectral indexes	Landsat	RGB + NIR + SWIR[4]	30	99
(Jiang et al., 2021)	Spectral index threshold	Sentinel 2	RGB + VRE1[5] + SWIR2	10 - 20	92.75 – 93
(Dong et al., 2022)	Spectral index threshold	Landsat / Sentinel 2	RGB + NIR + SWIR	30 / 20	97
(Basheer et al.,2022)	LULC – ArcGIS SVM	Landsat 8 / Sentinel 2 / Planet	RGB + Infrareds	30 / 10 / 3-5	89 – 94
(Y. Li et al., 2022)	Review of six Deep learning approaches	GF-2	RGB + NIR	4	96.36 - 97.27

Many studies use one of the mentioned methods in the study of J. Li et al. (2022). The most used method for waterbody extraction is a threshold method with a spectral index (multiband threshold method) (Table 2). These studies implemented this with the Normalized Difference Water Index (NDWI), which was assessed to be the fastest and most simple to implement (J. Li et al., 2022). This method builds upon the methods of Gao (1996) and Xu (2006) for computing the NDWI and of Otsu (1979) to split an image into two classes. Additional benefits of computing NDWI is that is can be used as additional feature in the classification models. Given this nature, most studies using classification algorithms also use the NDWI threshold method, indicated by the overlapping nature of previous studies in table 2 (Donchyts, Schellekens, et al., 2016; Dong et al., 2022; Vos et al., 2019).

---

[1] Red, Green, and Blue bands
[2] Near Infrared band
[3] Mid Infrared band
[4] Shortwave Infrared band
[5] Visible and near Infrared

Table 2 states that the accuracies of existing waterbody extraction are towards and over 90%. Most research is aimed on extracting large waterbodies. Only, Dong et al. (2022) aimed to test their method for small waterbodies, including shallow water streams. However, in contrast to their research aim, the authors decided to use images with a special resolution between 30 and 20 meters, which might not be adequate to extract small waterbodies, depending on the considered scale.

Classification accuracy (non-deep learning) with Red, Green, and Blue (RGB) bands along with either Shortwave Infrared (SWIR), Mid Infrared (MIR), or Visible and Near infrared (VRE1) gained accuracies between 89% and 95% (Basheer et al., 2022; Dong et al., 2022; Jiang et al., 2021; Thanh Noi & Kappas, 2017). In contract, the combination of RGB and Near-Infrared (NIR) gained accuracies between 82% and 90% (Mozgovoy et al., 2018). The availability of spectral bands depends on the specific platform and its spatial resolution, however this impacts spatial resolution (Table 2). This trade-off is also underpinned by the findings of Y. Li et al. (2022) stating that high-resolution spaceborne imagery comes with the challenge of having limited spectral information. From a Land Use Land Cover (LULC) prediction perspective, the accuracies mentioned are not based on the two-class distinction between water and non-water, however on a multi-class classification. From these approaches a support vector machine (SVM) predicting on pixel basis emerged as a promising model with accuracies between 90% and 95% (Basheer et al., 2022; Thanh Noi & Kappas, 2017).

Y. Li et al. (2022) reviewed similar methods as J. Li et al. (2022), however further studied the recent developments in deep learning waterbody extraction. Achieved accuracies are higher than other methods (Table 2). Y. Li et al. (2022) identified five key challenges for waterbody extraction based on high resolution spaceborne images: (1) Limited spectral information and small scene coverage, (2) variability of shape, size, and distribution, (3) scene complexity, (4) complex and blurry boundaries, and (5) deficiency of large-size image datasets. The fourth limitation is related to fact that water does not have straight and crisp edges, Large & Gilvear (2015) and Winterbottom & Gilvear (2000) had related arguments stating that their studies were limited by the challenge of overhanging vegetation, which obscured the riverbanks. These authors interpolated these vegetation patches by manually delineating a reasonable water edge.

Temporal resolution is an essential part of monitoring hydromorphology. The reviewed studies in Table 1 have temporal resolutions ranging from one yearly image to seven images across 87 years. Recent studies aimed to increase this and developed near real-time water mapping tools on spatial resolutions between 10 and 30 meters (Donchyts, Baart, et al., 2016; Donchyts et al., 2017; van Leeuwen et al., 2020). A key limitation of these methods as mentioned by the authors is the disability to detect small waterbodies due to the spatial resolution. High resolution open data sources, such as areal imagery or lidar scans, typically have temporal resolution in the range years. In contrast, Superview-1 data is available with both high spatial and temporal resolution between 2019 and 2023.

While the temporal resolution of existing riverbank erosion studies, beside the manual method from Hooke (1979) do not go beyond yearly (Table 1), opportunities to increase this have emerged with the Superview-1 data. This poses additional prospects for the monitoring of the KRW goals of hydromorphology, as both spatial and temporal resolution is of importance for monitoring. High temporal resolution waterbody monitoring for large waterbodies, as well as high spatial resolution hydromorphological monitoring based on aerial photographs and lidar scans are well-established in literature. However, there is a gap in knowledge regarding the monitoring hydromorphology of shallow water streams based on high temporal and spatial resolution, in combination with automated waterbody extraction, since classification accuracy for this is unknown. Specifically, images from the Superview-1 were used for this study as it provides the increased temporal resolution compared to other sources like Unmanned Aerial Vehicles (UAV) aerial photographs and lidar scans.

Based on the examined literature, a spaceborne remote sensing waterbody extraction approach emerges as a promising method for erosion monitoring. However, these methods needed to be tested to assess its accuracy. Therefore, this study aimed determine the classification accuracy of waterbody extraction methods based on Superview-1 images, with the goal to monitor hydromorphology of shallow streams on high temporal basis. For this, three methods for waterbody extraction were used (Otsu Threshold, single-image SVM and multi-image SVM). With regards to hydromorphological monitoring, the study area of the mouth of the Geul River was considered.

Sub questions to build towards the main question are:

1. What are the classification accuracies of the three tested waterbody extraction methods

2. What hydromorphological changes of the Geul River took place between 2019 and 2023?

2 DATA & METHODS

2.1 STUDY AREA

This study aimed to increase temporal resolution of hydromorphological monitoring with Superview-1 satellite images and assess its waterbody extraction classification accuracy. For this, the study area of the mouth of the Geul River was selected, which is located near Itteren (Limburg), the Netherlands. The Geul is a river with a catchment of 380 km^2 of which approximately 240 km^2 is in the Netherlands (de Moor & Verstraeten, 2008). The source of de Geul lies near the Belgium town Eynatten, making the total length of the river approximately 56 km (Leenaers, 1989).
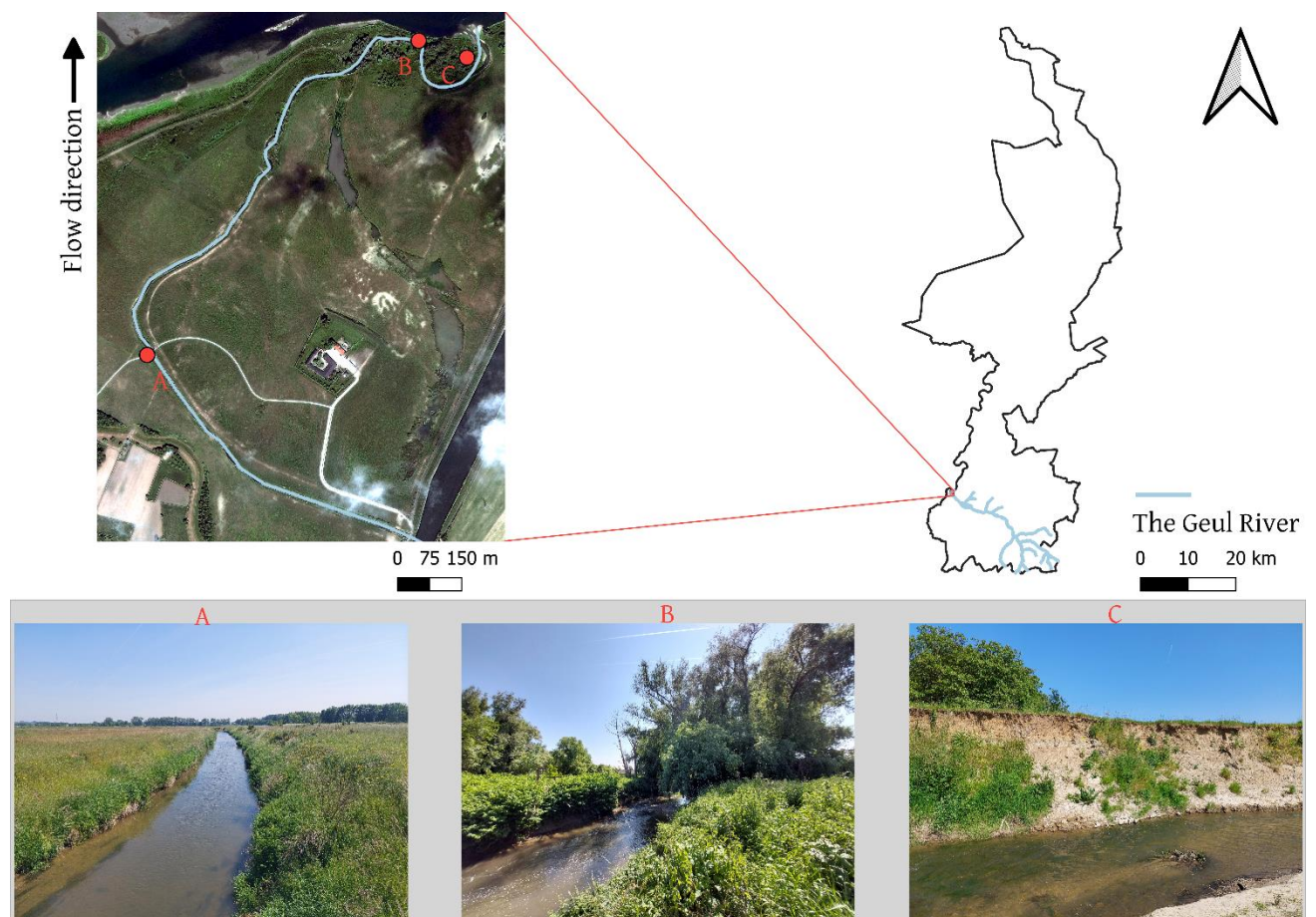
Fig. 1. Overview of study area, with on-site photographs. (A) upstream straight section, (B) downstream meandering section with overhanging vegetation, and (C) eroding bank near the mouth of the river.

The upstream part of the river, within the study area, consists of relatively straight river segments with limited vegetation adjacent to and above the river. Fig. 1 (A) shows an image of this section (image taken at (17759, 323524)[6]). The downstream part of the Geul River, near the mouth in the Maas River, shows a meandering part of the river with high vegetation around and above the river, shown in Fig. 1 (B) (image taken at (1781211, 324267)[6]). With the goal of hydromorphological monitoring, the mouth of the Geul River

---

[6] Coordinates in coordinate reference system Amersfoort / RD New, EPSG: 28992

presents an eroding bank, as shown in Fig. 1 (C) (image taken at (178374, 324226)[6]). Average width of the Geul river is around 8 to 15 meters, whereas the average discharge is 3.4 m^3 s^{-1} (de Moor, 2007; de Moor et al., 2007) The Geul River is considered a third/fourth order stream (Higler & Tolkamp, 1982).

In past years, the river is known for its ability to flood (van Heeringen et al., 2022). In 2021, the Geul River experienced two significant floodings. Bank erosion and channel displacement occur during such high discharge flooding events (Hooke, 1979; Rusnák & Lehotské, 2014; Winterbottom & Gilvear, 2000), making de Geul suitable study area for hydromorphology monitoring in the Netherlands.

2.2 DATA COLLECTION

2.2.1   SUPERVIEW-1 IMAGE DATA

The Superview-1 constellation consist of a collection of four commercial remote sensing satellites placed in a sun-synchronous orbit with an altitude of around 530 km. Superview-1 (01) and Superview-1 (02) were launched on the 28th of December 2016 (EOS-a, n.d.). On January 9, 2018, the last two satellites, Superview-1 (03) and Superview-1 (04) went to orbit (EOS-a, n.d.). The payload of the satellites are two sensors, one multispectral and one panchromatic.

In each of the satellites, the multispectral sensor measures the bands red, green, blue, and near infrared, the bandwidths and spatial resolutions are stated in Table 3. Additionally, a panchromatic sensor allowed for pan-sharpened red, green, blue, and near-infrared (RGBI) images with a spatial resolution of 0.5 meter. The process op pan-sharpening aims to combine the low-resolution data from a multispectral sensor with a high-resolution pan image to create a single high resolution colour image (Xie et al., 2021). These pan sharpened RGBI images were the input images for this study.

Table 3.
Overview of bandwidth and spatial resolution of the included bands of superview-1, derived from (SpaceWill, n.d.).

Spectral band	Bandwidth (nm)	Spatial Resolution (m)
PAN	450 - 900	0.5
Blue	450 - 520	2
Green	520 – 590	2
Red	630 - 690	2
NIR	770 - 890	2

The publisher of the Superview-1 images in the Netherlands, Netherlands Space Office (NSO), provides context on the processing that was performed on the Superview-1 images (NSO, n.d.). First, the raw satellite images were radiometrically calibrated. Radiometric calibration enables a relationship for converting the digital numbers of the images to radiance images with physical units (Liu et al., 2020). For the retrieved Superview-1 images this step adjusted for sun angle, view angle, and (particles in) the atmosphere (Helder et al., 2012; NSO, n.d.). The second pre-processing step involved sensor correction. Sensor correction typically consists of noise correction, radiance strength modification, wavelength dependent correction factor methodology, and lens distortion (Kelcey & Lucieer, 2012). An additional service of NSO is that they provide orthorectified images. Orthorectification is the process of correctly geo-locate image pixels (Campbell & Shin, 2012; Mercer et al., 2003).

NSO provides coverage of this data in the period between 2019 and 2023. Of the considered study area of the Geul, a total of 29 images were retrieved. The timeline in Fig. 2 shows the distribution of images over time.

The images were retrieved with the help of an application programmable interface (API). A script was created to extract these images. This script took a Geojson file of the desired study region, date range, and resolution. The API then downloads this data from the NSO organisation, which saved considerable time compared to manually downloading the files one by one.

2.2.2   LIDAR DERIVED VALIDATION POINT CLOUDS

Within the period of the collected Superview-1 images (2019-2023), three lidar campaigns were carried out. Data from this was retrieved in the form of .LAZ point clouds. One scan was completed by the National lidar database (Actueel Hoogtebestand Nederland, 2020). From flight plans, the date of the campaign was derived. The flight plan indicated that the AHN4 scan in the study area was completed on 18-12-2020 (AHN, 2020). The resolution of this data is a point density of between 10 –14 points per m² (AHN, n.d.-a).

Another organisation, Rijkswaterstaat, performed two additional scans of the area for their monitoring of the Maas River (Rijkswaterstaat, 2021, 2022). Metadata of the Rijkswaterstaat scan reveals that the provided scans have resolution of 16.6 points per m². These campaigns were carried out on 10-04-2021 and 07-04-2022.

The retrieved point clouds where output of the classification algorithm performed by the respective organizations. Hence, points in the point cloud were either classified as: ground, buildings, miscellaneous, or water (AHN, n.d.-b). Although water is a class in their classification, not all water was classified in their classification, due to the reflective nature of water (Paul et al., 2020; Saylam et al., 2017). Therefore, water surfaces appear as missing data in the retrieved point clouds. Although missing data in lidar point clouds can have multiple causes such non-overlapping flight strips, given the full coverage of the point cloud, the missing data patches were assumed to be the Geul River. This extraction from the point clouds was visually inspected to be following the riverbanks.

Past studies have substantiated the accuracy of lidar classification methods (Antonarakis et al., 2008; Yan et al., 2015). One study summarized the accuracies of those studies, which range between 66% for older methods and >90% for more recent studies (Yan et al., 2015). A specific study focussed on river areas, achieved an overall classification accuracy between 94% and 95% (Antonarakis et al., 2008). Additionally, the height accuracy of the lidar scans is known to be within 15cm in 95,4% of the data points (AHN, n.d.-b). While the exact method used by AHN is not clear from a technical point of view, newer lidar classification methods can be seen as reliable validation sources for extracting water surfaces.

2.2.3   DATA PRE-PROCESSING

Image pre-processing
The retrieved Superview-1 images were first clipped on the study area. Additionally, the Normalized Difference Water Index (NDWI) and Normalized Difference Vegetation Index (NDVI) were computed for the waterbody extraction methods. The NDWI (eq. 1) is an index designed for creating contrast with water (Gao, 1996; Xu, 2006). The NDVI (eq. 2) revolves around the same idea for contrast on vegetation (Myneni et al., 1995).
For the analysis mentioned in section 2.3.1, the NDWI was used. For the analysis mentioned regarding the classifiers (sections 2.3.2 and 2.3.3), an enhanced version of the RGBI raster was used by adding the NDWI and NDVI rasters as bands as one multi-dimensional raster dataset. Adding these spectral indices as bands is known to increase classification accuracy (J. Li et al., 2022).

$$NDWI = \frac{Green - NIR}{Green + NIR} \quad (eq. 1)$$

$$NDVI = \frac{NIR - Red}{NIR + Red} \qquad (eq.\,2)$$

Lidar pre-processing
The workflow to convert lidar to raster consist of three key steps. The first step is to convert the classified lidar .Laz file to a .las file to be compatible with ArcGIS pro functionalities. The second step was to convert the point could to a digital elevation model (DEM) at a spatial resolution of 50cm. Because of the low reflectance properties of water, the Geul River was retrieved by the NoData pixels. The third step was to polygonise the raster image. The river polygon could be extracted by means of an intersect operation on a defined water point in the river.

2.3 METHODS

The Superview-1 images were used for the waterbody extraction and hydromorphological monitoring whereas, lidar validation point clouds were used as a reference for computing the accuracy of the waterbody extraction methods. Both images and lidar scans are collected of the study area between the period of 2019 and 2023 (Fig. 2).
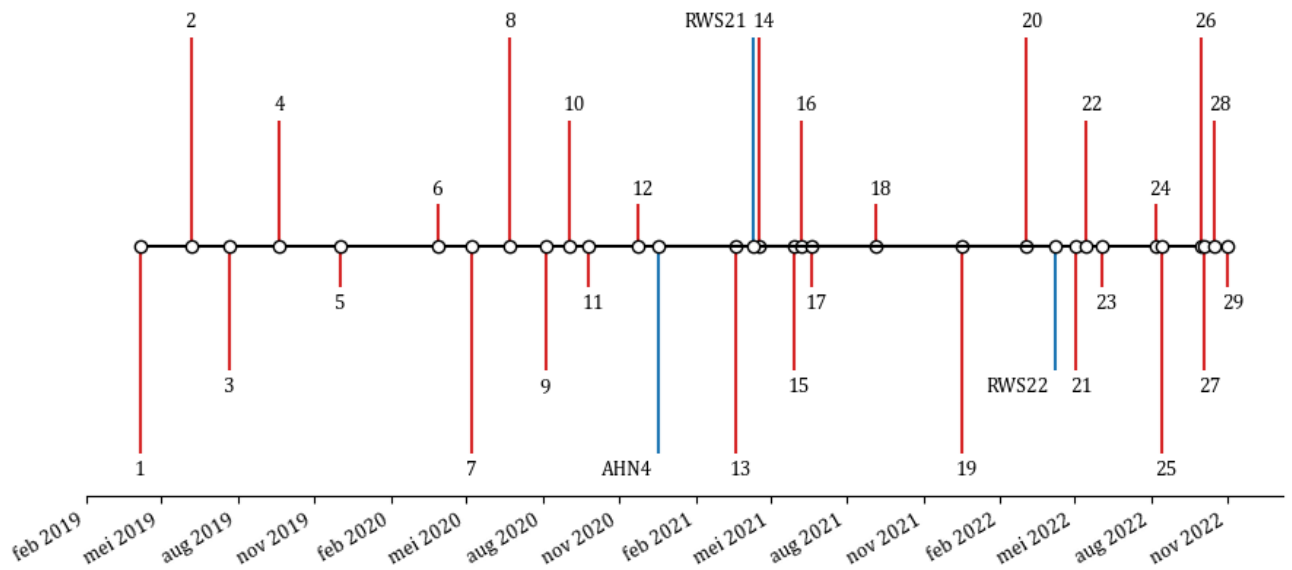
Fig. 2. Timeline of the collected Superview-1 images (red) and lidar point clouds (blue). Numbers indicate the count of superview-1 images. Codes associated with the blue lines are related to the data source; AHN4 (Actueel Hoogtebestand Nederland, 2020), RWS21 (Rijkswaterstaat, 2021), and RWS22 (Rijkswaterstaat, 2022b).

The objective of this research can be split into two main sub goals. After data retrieval and pre-processing, the first subgoal is to compute the accuracy of waterbody extraction with Superview-1 images, reflected in the waterbody extraction assessment phase (Fig. 3). The second subgoal related to the main objective of this research is to perform hydromorphological monitoring of a shallow water stream, which is reflected in the hydromorphological monitoring phase (Fig.3).

Three methods are included for testing the accuracies of different waterbody extraction methods (Fig. 3). The methods for this research were selected based on the literature review. The Otsu threshold method emerged as a feasible implementation for waterbody extraction (Table 2). Moreover, the LULC implementation of the support vector machine appeared feasible implementation. While deep learning was labelled as the best

performing method type, with the highest achieved accuracies, due to time limitations these implementations had to be moved to suggestions for further research.
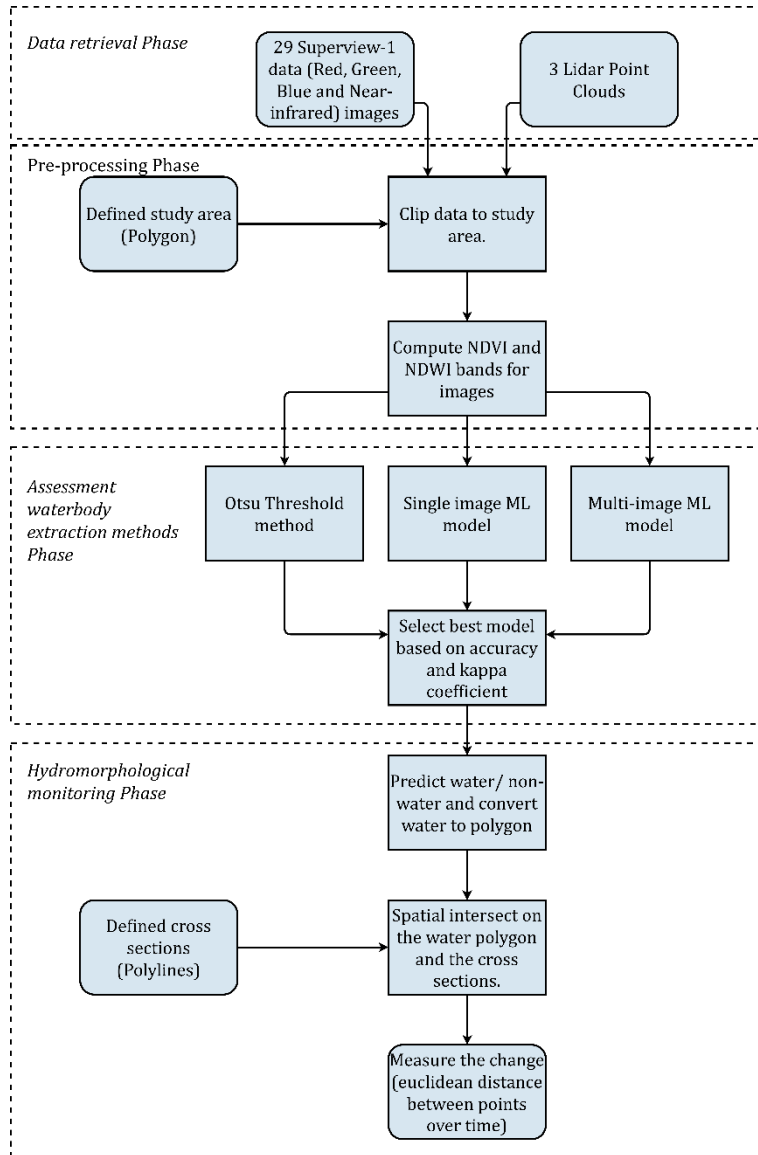

Fig. 3, *Schematic overview of included methods in this study and explaining the different phases included.*

2.3.1 THRESHOLD METHOD

The Otsu threshold method was proven to be an effective solution for waterbody extraction (Donchyts, Schellekens, et al., 2016; Dong et al., 2022; Langat et al., 2019; Mozgovoy et al., 2018; Vos et al., 2019). The idea of this method is to minimize the intraclass distribution and maximise the interclass distribution of values. This method splits an image in two classes. In the reviewed papers, this method implemented with the NDWI index. Multiple variants of NDWI with different spectral bands exist, by including different spectral bands. For this research the version using the NIR band (eq. 1) was used because of the availability in bands. Other variants of the NDWI use the bands MIR and Green, which are available on other spaceborne remote sensing platforms such as Landsat and Sentinel however not on the Superview-1 (Xu, 2006). The index is designed to create contrast between water and non-water surfaces. One source indicates that values between 0.2/0.0 and

1 indicate water, while values between -1 and 0 indicate non-water surfaces (EOS-b, n.d.). This method however does not consider differences between individual images. In contrast, the threshold method relies more on contrast between the two classes instead of absolute values. The implementation of this method was done in the GIS software ArcGIS pro with the Binary Thresholding function (Esri, n.d.).

2.3.2 SINGLE-IMAGE PIXEL-BASED SUPERVISED LEARNING METHOD

Land-use land cover classification methods commonly use a pixel-based implementation of a classification model. Proven models had accuracies between 89% and 94% (Talukdar et al., 2020; Thanh Noi & Kappas, 2017). Between supervised learning methods there is a division between pixel based and object based. One study identified that for small waterbodies, pixel based is the most suitable option (J. Li et al., 2022). In these studies, the Support Vector Machine (SVM) emerges as best performing model. Such SVM model requires labelled data to train on. The concept of a SVM is based on the structural risk minimization criteria to find the optimal classification hyperplane in the high-dimensional feature space (J. Li et al., 2022; Mountrakis et al., 2011; Talukdar et al., 2020).

Manual delineation of classes on the Superview-1 images was performed to serve as input for the training data in ArcGIS pro. For this research, a total of four classes were considered. The first two are the classes River and Ground. The remaining two classes are more focussed on the problem of overhanging vegetation, as identified in past research to be a specific problem for shallow water streams. Therefore, overhanging vegetation was considered a class during labelling of data. Because this class is spectrally similar to regular tree canopies, trees were also considered a class. After prediction, the classes are combined to the parent classes water (river + overhanging vegetation) and non-water (ground + vegetation).

The input for this model is the RGBI image, enhanced with NDWI and NDVI bands. This adding was suggested by earlier studies as it aims to increase the accuracy of the model (J. Li et al., 2022). The included model is the ArcGIS pro implementation of a Support Vector Machine as past research indicated the high performance in benchmarks, compared to other implementations (Basheer et al., 2022). The ArcGIS pro implementation of used 250 samples of each of the included classes, ensuring a balanced class division. One model was made for each of the three analysis images because of ArcGIS implementation only being able to accept one image as training data, resulting in a total of three models. Models could not be used on images due to spectral differences, hence three models were made for each of the validation images.

2.3.3 MULTI-IMAGE PIXEL-BASED SUPERVISED LEARNING METHOD

Recent studies identify the challenge of seasonal change in images, resulting in different spectral values (Cheng et al., 2014; Dong et al., 2022; Lu et al., 2019). This creates challenges for multi-temporal analysis as the model trained on one image might not be suitable for another image. This was also found with the single-image SVM model. To cope with this one study only collected data from the same seasons (Zewdie & Csaplovics, 2015). Another study study trained the SVM model on multiple images (Ahmad et al., 2010). As the aim of this study was to increase temporal resolution of hydromorphological monitoring, the challenge of spectral differences between images due to seasonal changes became a problem, which could not be tackled with training the model a single image. To overcome this challenge, this method used training data from multiple images to train one model. This incorporated the spectral information of multiple images, instead creating models that are only suited for one specific image, like done with the single image method.

The input for this model consisted of seven randomly selected images in different seasons for training, incorporating different seasons and circumstances into the training data. The Supervieuw-1 images used for validation were not used for the training of the model, to test the model on unseen data. For the seven

selected images, manual landcover classes were delineated. The same training classes as the single-image model were used for training. For this implementation, the NDVI and NDWI values were scaled towards the same scale of the RGBI images, in order to overcome problems with the classification model.

The images were transformed into a Pandas DataFrame with the rows representing the labelled raster cells and the columns representing the spectral bands and the class label. This made it possible to merge the spectral Dataframes of different images into one training dataset. Based on the reflective values of the merged images, a SVM model was trained. A 0.5 fraction, based on the amount of training samples in every image, of the full available data was used to limit the size of the training dataset. This ensured that every class appeared in proportion to the amount of collected training samples, avoiding that a small class as overhanging vegetation becomes dominant.

Implementation of this was done with the scikit-learn SVM (Pedregosa et al., 2011). The model takes three key hyperparameters which have significant influence on the accuracy of the model. The parameters the SVM model requires are the kernel, C, and max iterations. From literature it is known that the radial kernel, performs best for remote sensing classification (Lu et al., 2019; Talukdar et al., 2020; Thanh Noi & Kappas, 2017; Zewdie & Csaplovics, 2015). The radial kernel allows for non-linear classification (Razaque et al., 2021). For this study, optimal parameters were found with hyperparameter tuning, implemented with gridsearchcv from scikit learn. The majority filter (four neighbours; majority criteria) was additionally used to remove false classifications, so that isolated pixels do not exist.

The prediction phase was implemented in a similar manner as the training phase. The rasters to be classified were transformed to a Pandas DataFrame. By leveraging Dask arrays, predictions were performed with multicore processing, resulting in faster computation time and allowing for scalability of the method (Rocklin, 2015).

2.3.4 PERFORMANCE MEASURES

With regards to sub question one, the selected three waterbody extraction methods were assessed based on the performance measured against the lidar validation scan. Of the 29 analysis images, the images closest in time to the validation lidar scan are paired (Table 4. & Fig.4)

Table 4
Superview-1 image and lidar point cloud pairs for assessing the accuracy and Kappa of waterbody extraction methods.

Image date	Validation lidar scan date
20-03-2021	18-12-2020
17-04-2021	10-04-2021
02-05-2022	07-04-2022

Fig. 4. Overview of the three Superview-1 images of the study area, selected for the waterbody extraction methods assessment.

For the sake of comparison, the assumption was made that water levels between the analysis images and lidar scans are similar. This assumption allows for the implicit statement that the riverbanks are at the same location between analysis image and validation scan.

Each method was used to make a binary prediction on the classes water and non-water. For all three methods, and the considered test images, a confusion matrix was generated within a 15-meter buffer of the validation river. The performance measure to compare the included methods is the accuracy. The accuracy is based on the confusion matrix accuracy of the sum of True Positives (TP) and True Negatives (TN) divided by the sum of TP, TN, False positives (FP), and False Negatives (FN) (eq. 3).

$$Accuracy = \frac{TP + TN}{TP + TN + FP + FN} \quad (eq.\,3)$$

Additionally, the Cohen's Kappa coefficient was also included to assess the best performing method (eq. 4) (Cohen, 1960; sklearn, 2023). This measure is the proportion of agreement corrected for chance (Warrens, 2015). This measure is well acknowledged by the RS community (Feizizadeh et al., 2022) .

$$Cohen's\ Kappa = \frac{p_0 - p_e}{1 - p_e} \quad (eq.\,4)$$

Where p_0 is the empirical probability of agreement on the label assigned to any sample, and p_e is the expected agreement when both annotators assign labels randomly (sklearn, 2023).

Additionally, for all three waterbody extraction methods a north section (around the eroding section) and south section (around the non-eroding section) are plotted for visual reference (Fig. 11 – Fig. 16). Accuracy of overhanging vegetation could not be computed as the data of the validation scan only included the classes water and non-water. Therefore, performance of the overhanging vegetation classification was interpreted manually with the maps.

2.3.5 HYDROMORPHOLOGICAL MONITORING

With regards to sub question two, the hydromorphological monitoring was performed at two subsections of the study area, including one eroding section and one non-eroding section (Fig. 5.). Identifying a shifting riverbank is evenly important as having a non-eroding bank showing no channel shift. The method of

hydromorphological monitoring which was used for this study is based on the shift of the waterbody with respect to a selection of pre-defined cross sections. Existing research also used cross sections, in the form of height profiles (Hemmelder et al., 2018). Points of interest on this cross section is the left bank, centre point and right bank. For both the eroding section and the non-eroding section, four cross sections at each site are defined (Fig. 5)

Fig. 5. *Overview of the hydromorphological monitoring sites (eroding and non-eroding), with the cross sections (red).*

Using the best performing waterbody extraction method, this study created predictions on the rasters of the specific monitoring sites. The resulting classified raster with the distinction of water and non-water were then polygonised. The images with cloud cover above the monitoring site were automatically filtered from the analysis. Additionally, falsely classified river polygons were filtered out by removing outliers in terms of polygon area. The polygons were plotted to gain spatial insight into both the dynamics of the river and the classification predictions. Additionally, Intersecting the river polygon with the cross sections gave two points at either bank of the river. To determine the centre point, the location of the two banks are averages. Using this point data, the Euclidean distance of the specific point of interest was computed over time, enabling the visualization of the river shift over time.

3 RESULTS

3.1 WATERBODY EXTRACTION ASSESSMENT

3.1.1   OTSU THRESHOLD RESULTS

From the Otsu threshold method, the Accuracy and Kappa coefficient were an average of 90% and 0.70, respectively (Table 5). Of the three measuring moments, the image of 20-03-2021 gave the highest accuracy, followed by 05-05-2022 and 17-04-2021. Additionally, the extracted rivers were plotted along with the validation scan for the three measuring moments in appendix I (Fig.11 & Fig.12). The predictions of the eroding section (Fig. 11) show a patchy pattern compared with the validation image. This section contains high vegetation above or adjacent to the river (Fig. 1 & Fig. 4.). Furthermore, in the 17-04-2021 prediction (Fig.11), a large amount water was predicted compared to the validation image due to cloud shadow (Fig.4). This also reflected in the amount of FP water observations of the 2021 image (Table 7). In Table 6 until Table 8, the confusion matrices of the three images can be found.

Table 5
Accuracies and Kappa coefficients of the Otsu threshold method.

Date of image	Accuracy (%)	Kappa coefficient
20-03-2021	92	0.75
17-04-2021	88	0.66
02-05-2022	91	0.70
Average	**90**	**0.70**

Table 6
Confusion matrix of the Otsu threshold method of the 20-03-2021 image.

		Prediction	
		Non-Water	Water
Validation	Non-Water	251038	22143
	Water	6435	59306

Table 7
Confusion matrix of the Otsu threshold method of the 17-04-2021 image.

		Prediction	
		Non-Water	Water
Validation	Non-Water	239034	32631
	Water	9763	60155

Table 8
Confusion matrix of the Otsu threshold method of the 02-05-2022 image.

		Prediction	
		Non-Water	Water
Validation	Non-Water	263627	9237
	Water	21704	48732

3.1.2 SINGLE-IMAGE SUPPORT VECTOR MACHINE RESULTS

The second tested method, the pixel based SVM method trained and predicted on the same image gained an average accuracy of 76%, whereas the Kappa coefficient gained an average of 0.50 (Table 9.). The best performing model of the three was the 17-04-2021 model on the respective image. The 02-05-2022 model and image and 20-03-2021 model and image both had lower accuracies and Kappa coefficients.

Fig. 13 and Fig. 14 in appendix I show the predicted images compared to the lidar validation for the eroding section. This image shows a patchy pattern of water and non-water. Fig.13 and Fig. 14 regarding the non-eroding section for 20-03-2021 shows more predicted water compared to the validation image, as reflected in table 9. Also, most of the prediction images show that more of the overhanging vegetation was classified with this method. However, this was not without the expense of FP water predictions (Fig. 13 & Table 11) The confusion matrixes of the individual images can be found in Table 10 to 12.

Table 9
Accuracies and Kappa coefficients of the Single-image SVM method.

Date of image	Accuracy (%)	Kappa coefficient
20-03-2021	55	0.19
17-04-2021	91	0.75
02-05-2022	82	0.55
Average	**76**	**0.50**

Table 10
Confusion matrix of the single-image SVM method of the 20-03-2021 image.

		Prediction	
		Non-Water	Water
Validation	Non-Water	131025	14156
	Water	9056	65585

Table 11
Confusion matrix of the single-image SVM method of the 17-04-2021 image.

		Prediction	
		Non-Water	Water
Validation	Non-Water	250185	21480
	Water	8591	61327

Table 12
Confusion matrix of the single-image SVM method of the 02-05-2022 image.

		Prediction	
		Non-Water	Water
Validation	Non-Water	21687	58177
	Water	5059	65377

3.1.3 MULTI-IMAGE SUPPORT VECTOR MACHINE RESULTS

Training data for the third selected method contained the feature space as shown in Fig. 6. It shows the distribution of the training data across the different bands. The feature space of the training data contains approximately 95,000 rows, and six features for prediction.
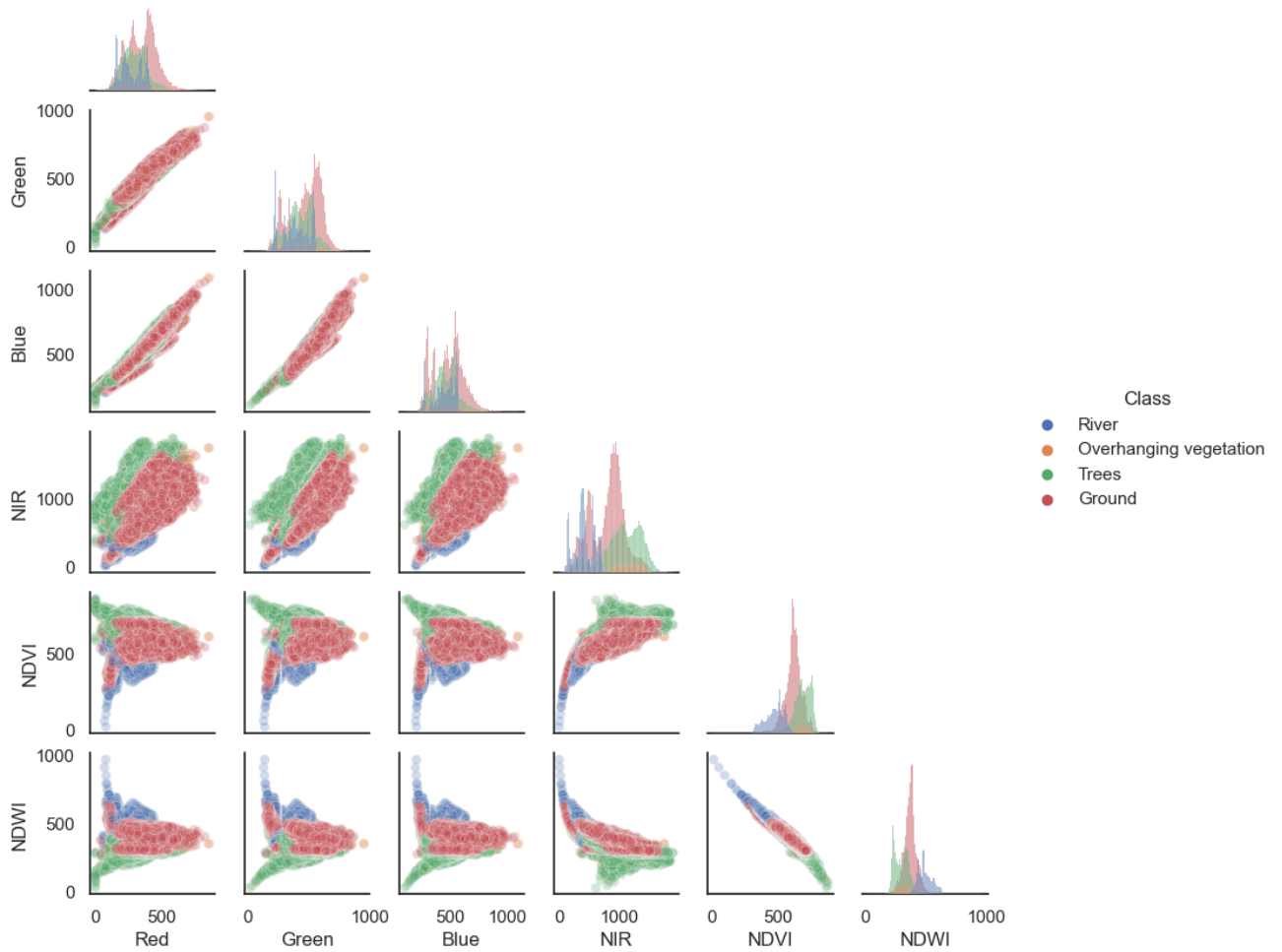
Fig. 6, *feature space of the training dataset of the multi-image SVM model.*

This multi-image model gained an average accuracy of 90%, Table 13 further specifies the accuracies of all the specific test images. Tables 14 to 16 show the confusion matrices of the specific images.

Table 13
Accuracies and Kappa coefficients of the Otsu threshold method.

Date of image	Accuracy (%)	Kappa coefficient
20-03-2021	94	0.80
17-04-2021	84	0.61
02-05-2022	92	0.75

	Average	90	0.72

Table 14

Confusion matrix of the multi-image SVM method of the 20-03-2021 image.

		Prediction	
		Non-Water	Water
Validation	Non-Water	261715	11569
	Water	10215	55432

Table 15

Confusion matrix of the multi-image SVM method of the 17-04-2021 image.

		Prediction	
		Non-Water	Water
Validation	Non-Water	222171	49580
	Water	4427	65489

Table 16

Confusion matrix of the multi-image SVM method of the 02-05-2022 image.

		Prediction	
		Non-Water	Water
Validation	Non-Water	258325	14373
	Water	14184	56259

Fig. 15 & Fig. 16 in appendix I shows the predicted and ground truth images for the third method. It reveals that the 20-03-2021 and 02-05-2022 image there is a patchy pattern in Fig. 15, whereas Fig. 16 shows more crisp lines. The 17-04-2021 image shows a significant portion of water pixel in the north part (Fig. 15).

## 3.2 HYDROMORPHOLICAL MONITORING AT THE MOUTH OF THE GEUL RIVER

Based on the performance of the included models, and further arguments stated in section 4, the hydromorphological monitoring was performed based on the multi-image SVM model. Between fifteen and seventeen polygons were extracted, depending on the specific cross section. The extracted polygons of the eroding section were plotted to visually interpret the shift of the river (Fig. 7). Approximately two of the predicted polygons show large uncertainty in the boundary of the river, with large additional predicted water.
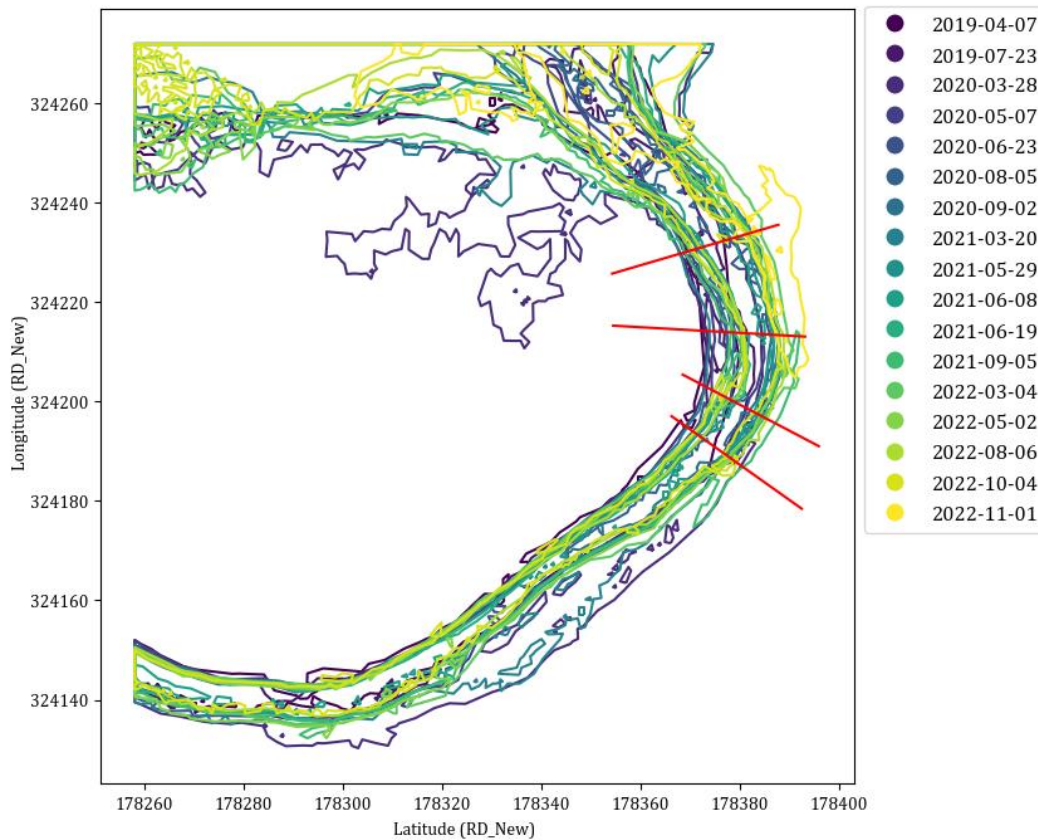
Fig.7. *Extracted polygons over time of the used superview-1 images for hydromorphological monitoring on the eroding section. Cross sections are delineated in red.*

Furthermore, the cross sections of the eroding section showed a total centre point shift between 4.5 and 8.6 meters throughout the study period (Fig. 8). Left bank shift was between 1,4 and 8.6 meters whereas the right bank shift was between 4.6 and 8.6 meters throughout the study period. Furthermore, maximum bank right bank shift was recorded of 13.1 meters on the second cross section.

The first, second and third cross sections show clear temporal trends in channel shift (Fig. 8). The fourth eroding cross section shows less of a trend.
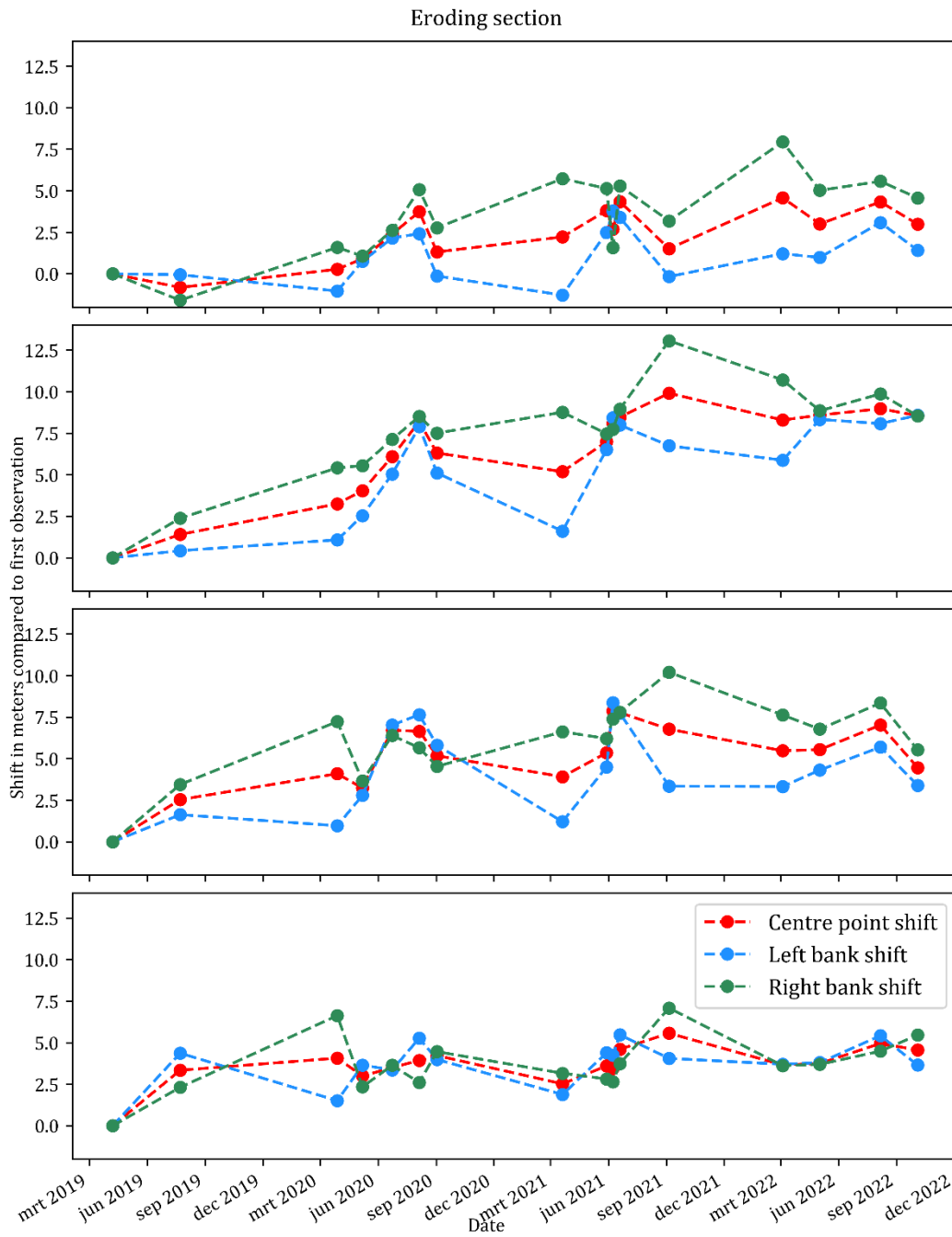
Fig. 8. *Temporal plot of the shift of the centre point and left and right riverbanks of the eroding section. Shift is measured compared to the first observation.*

The river in the non-eroding section remained on the same location, however one outlier in right riverbank was shown (Fig. 9.). Over time, no clear trend was derived from Fig. 9.
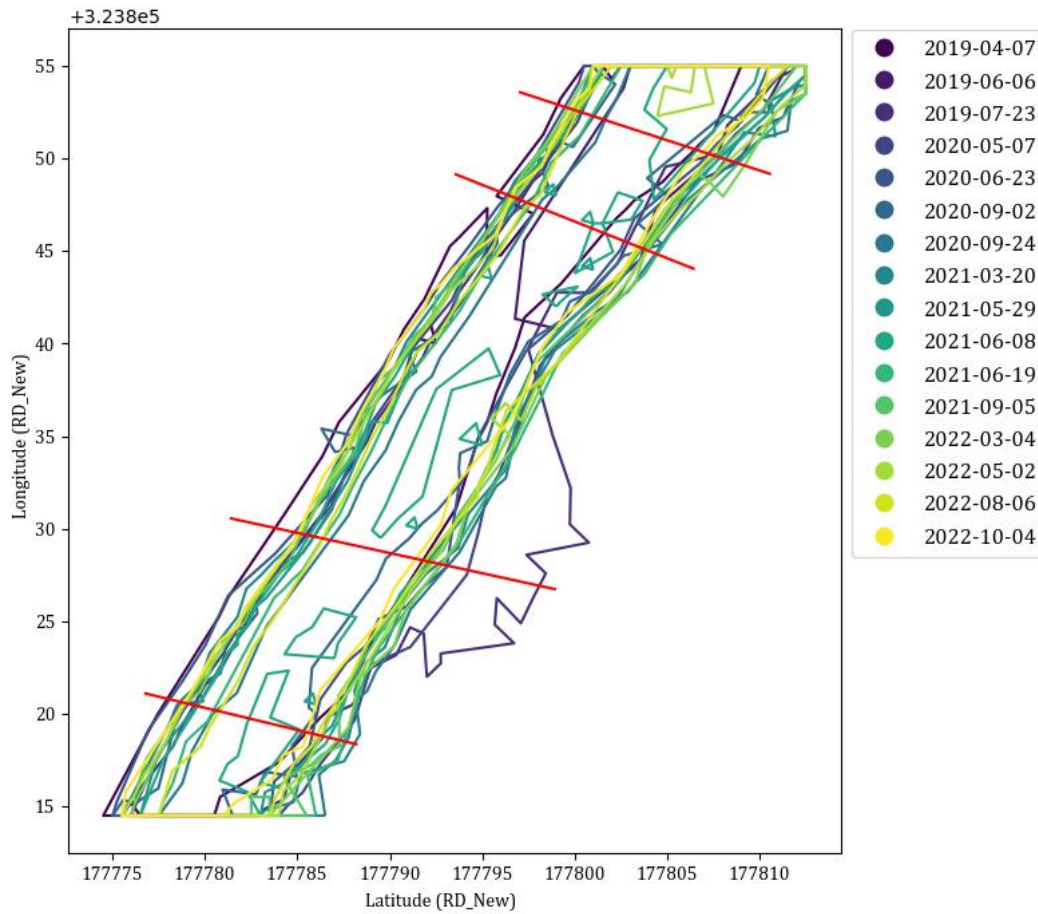
Fig.9. *Extracted polygons over time of the used superview-1 images for hydromorphological monitoring on the non-eroding section. Cross sections are delineated in red.*

Plotting the temporal riverbank shift (Fig. 10) showed no shifting trend on the non-eroding section. Maximum riverbank shift was recorded of 6.4 meters which was due to a classification error resulted by shadow. However, this was due to shadow. Overall, the centre point of remained between 0.2 and 1.3 meters of shift during the study period. The left bank shift was between 0.7 and 1.3 meters towards the end of the study period. The right bank shift remained between -0.4 and 1.9 meters at the end of the study period.
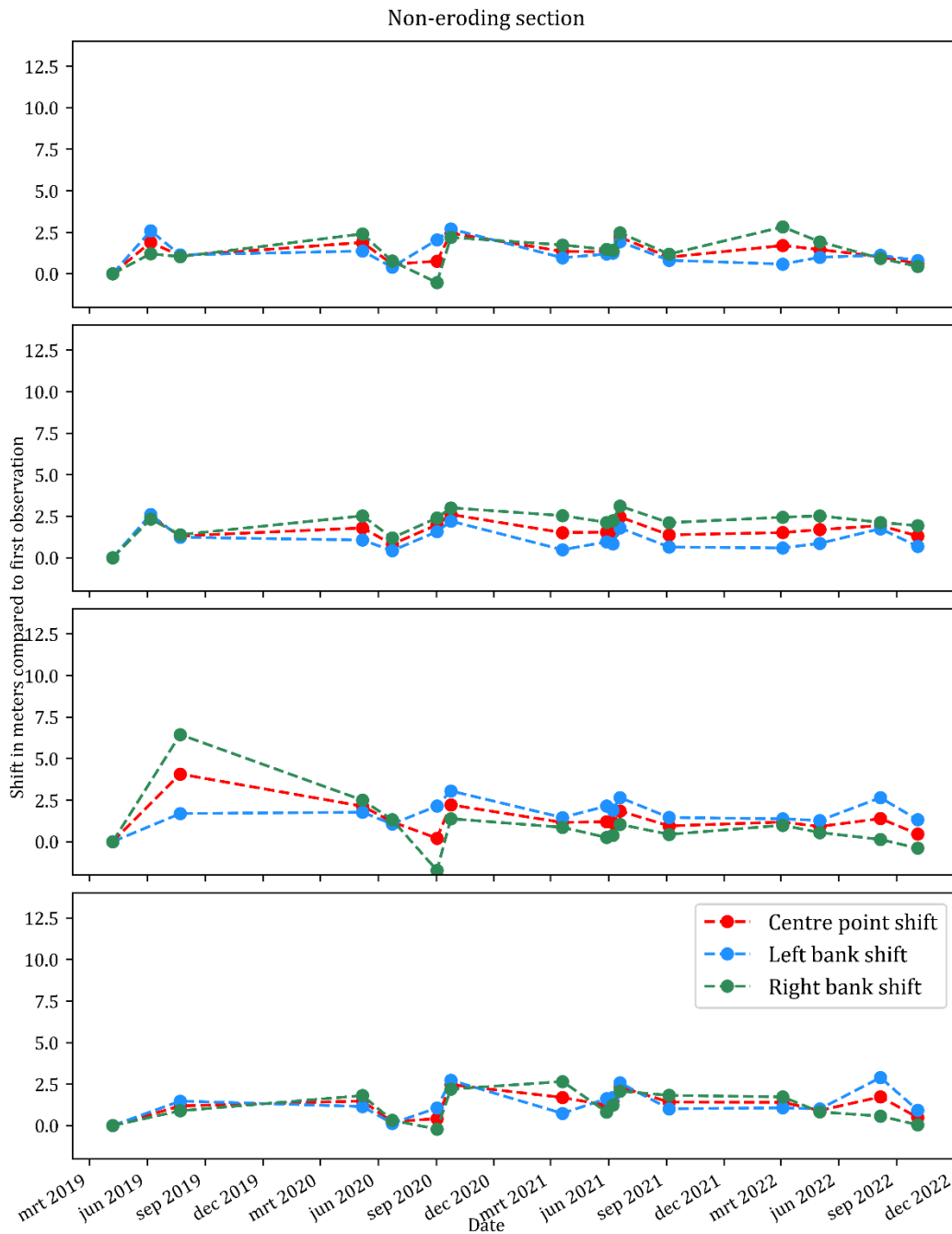
Fig. 10. *Temporal plot of the shift of the centre point and left and right riverbanks of the non-eroding section. Shift is measured compared to the first observation.*

For both the eroding and non-eroding sections of the analysis gif animations were created to visualize the polygons and the Superview-1 images over time. These gifs can be found on GitHub.

4 DISCUSSION

This study aimed to assess which waterbody extraction method gained the highest accuracy with Superview-1 images, compared to lidar scans to be able to monitor the hydromorphology of shallow river systems. The motivation to do this is related to the goals of the WFD. The definition of the WFD for hydromorphology omits the time component, deemed important by (Newson et al., 2006; Vogel & Asce, 2011). Therefore, this study went beyond the definition of WFD and build further upon the necessity of monitoring hydromorphology in terms of erosion and sedimentation processes. This research created a method for measuring this change in morphology with Supeview-1 images, to create more hydromorphological context on high temporal basis of shallow river ecological systems.

The Otsu threshold method demonstrated high accuracy, especially considering its complexity. This finding was consisted with research (Donchyts, Baart, et al., 2016; Dong et al., 2022; Jiang et al., 2021; Langat et al., 2019; J. Li et al., 2022; Mozgovoy et al., 2018; Vos et al., 2019). Average accuracy was 90%, with a Kappa coefficient of 0.70. However, this method was sensitive for misclassification regarding the cloud shadow in the 17-04-2021 image, as well as for the overhanging vegetation near the eroding section of the stream (Fig. 11).

The single-image SVM method had the lowest accuracy of the tested methods with 76% (Kappa 0.50). howe er, this model successfully addressed one of the key limitations identified from literature, overhanging vegetation (Large & Gilvear, 2015; Winterbottom & Gilvear, 2000). Nevertheless, this could not be identified with both the threshold method and the multi-image methods, reflected by the patchy patterns (Fig.11 & Fig. 15). While the single image model was able to detect overhanging vegetation, it was not able to do this without the expense of creating false positive observations of this class as well. This resulted in a lower classification accuracy on water vs non-water, as reflected in table 5. Therefore, the limitation of overhanging vegetation was still left a challenge with regard to spaceborne remote sensing. The presence of cloud shadow in the 14-07-2021 image was not a problem for this model, as it was trained on the spectral properties of the specific image.

Increasing temporal resolution of images also introduced the problem of seasonality in spectral values. Earlier temporal research collected their imagery in the same season, to overcome this challenge (Zewdie & Csaplovics, 2015). The single image model could not cope with differences between images. Therefore, this study opted to train a classification model spectral values from multiple images in various seasons, to create a generalized model. This method resulted in a classification accuracy of 0.90 with a Kappa coefficient of 0.72. In the feature space, there is significant overlap between classes within most of the histograms (Fig. 6). However, given the number of features, the SVM is able to extract the different classes. Overhanging vegetation was a problem for this model, shown by the patchy pattern in Fig. 15. Also, the model was not able to cope with the cloud shadow of the 17-04-2021 image.

In terms of accuracies, this study gained comparable accuracies on waterbody extraction as recent studies using spectral thresholding (Dong et al., 2022; Jiang et al., 2021; Mozgovoy et al., 2018). Past studies gained accuracies between 82% and 97%, whereas this study gained average accuracies between 90%. Moreover, comparing the Support Vector Machine accuracies, the single image performed worse than literature with its 76% accuracy. Existing studies with Support Vector Machines archived accuracies in the range of 90 - 95% accuracy. Nevertheless, the multi-image Support Vector Machine realized accuracies in line with the existing studies with its 90% accuracy. Though in line, the 90% is at the lower side of the accuracy range. Additionally, comparing the accuracies computed by past studies using deep learning (96.36% - 99%), the results of this research were lower. From this study overhanging vegetation and cloud shadow emerges as key limitations for shallow water stream waterbody extraction, impacting the accuracy negatively. This explains the fact

that the classification accuracies of this study were lower than existing studies. lower waterbody extraction accuracy.

Based on classification accuracies, both the Otsu threshold method and the multi-image method gained the 90%, the difference is that the multi-image model had a higher Kappa coefficient. Therefore, the decision was made to continue with the multi-image model for the hydromorphological monitoring.

Not all retrieved images were used for hydromorphological monitoring. Between fifteen and seventeen images, depending on the specific cross section, of the total of 29 images were used for monitoring due classification errors or cloud cover obstruction. Hence, making the average temporal resolution of this study around five yearly images.

The hydromorphological change between 2019 and 2023 along the eroding cross sections was striking. The right bank of the eroding section experienced a maximum bank shift between 7.6 and 13.1 meters. At the end of the study period a total centre point shift was measured of between 4.5 and 8.6 meters. From the temporal plots, a clear shifting trend was derived (Fig. 8). The non-eroding section shifted less than the eroding section with between 0.2 and 1.3 meters for the centre point. Maximum shift for the non-eroding section was dominated with a miss classified section, highlighting the that the classification accuracy is highly important for quality monitoring. However, regardless of the included misclassification, no eroding trend was found in the temporal plots of the non-eroding section (Fig. 10).

Compared with the study of Langat et al. (2019), this research revealed rather insignificant changes in river morphology. In contrast, compared with other shallow water streams of Hemmelder et al., (2018), Hooke (1979), and Winterbottom & Gilvear (2000), findings are comparable. The temporal resolution of hydromorphological monitoring of the reviewed river specific studies, was between one image yearly and one image every twelve years. This study was able to increase this resolution to five yearly images. While (Donchyts, Baart, et al., 2016; Donchyts et al., 2017; van Leeuwen et al., 2020) provide a high temporal resolution with near real time waterbody mapping, the spatial resolution of 10 or 30 meters is not adequate for shallow water steams.

From a perspective of feasibility of monitoring on high temporal basis, spaceborne remote sensing created a clear advantage compared to UAV data as used by Hemmelder et al. (2018). Spaceborne remote sensing eliminates the additional resources of UAV equipment and operators. However, hydromorphological monitoring with spaceborne remote sensing compromises on spatial resolution and three-dimensional capabilities.

A key assumption of this study was that the difference in water level between Superview-1 images and validation scans was insignificant. For the mouth of the Geul River, the water level is influences by the water level of the Maas River. The actual water levels on the specific days differed (Table 17). Also, throughout the days of which data has been retrieved, waterlevels fluctuated.

Table 17
Overview of water level of the Maas River near the mouth of the Geul River, at location Borgharen Dorp, retrieved (Rijkswaterstaat, 2023).

Date of image	Average water level of the Maas River in cm above NAP	Date of lidar	Average water level of the Maas River in cm above NAP	Absolute difference in cm
20-03-2021	4082 ± 118	18-12-2020	4033 ± 117	49
17-04-2021	4019 ± 117	10-04-2021	4025 ± 118	6
02-05-2022	3836 ± 14	07-04-2022	3893 ± 16	57

This water level difference most definitely influenced the accuracy negatively, as riverbank locations differ between the superview-1 images compared to the validation scans. It must be noted that a perfect situation would be to have a lidar scan on the same exact moment of the satellite image, resulting in equal environmental circumstances. This was however not feasible to arrange for this study.

Two key limitations related to the waterbody extraction of this approach for hydromorphological monitoring were identified. Firstly, The limitation of cloud shadow was identified. In this analysis, the north part of the 17-04-2021 image was subject to cloud shadow (Fig 4). Results indicate that only the model trained on this single image data was able to cope with this. The Otsu threshold and Multi-image SVM approaches confused this shadow area to be water. This limitation was also found in the review by Y. Li et al., (2022). There are approaches available to mask these cloud shadows (Shahtahmassebi et al., 2013). Additionally, cloud shadow classes could be predicted with additional classes in the SVM. However due to time limitation, these must be explored in further research. Secondly, the limitation of overhanging vegetation was identified. Because the multi-image SVM method is currently not able to detect this, the usability of the method is biased towards open water surfaces. However, hydromorphological monitoring is equally important in these overhanging vegetation sections compared to open sections and must not be ignored.

Further studies should research methods to extract water under patches of overhanging vegetation, and compute its accuracy. One suggestion is to the method proposed by Zeng et al. (2015) to interpolate the river at patches over overhanging vegetation. This method connects the discontinued river patches with the assistance of an image pyramid (Zeng et al., 2015). Furthermore, to limit the false positive overhanging vegetation predictions, multi-temporal techniques such as dynamic Bayesian network can produce probabilistic reasoning, which could assist detecting false positives (Jianya et al., 2008). Another suggestion is to leverage data fusion opportunities to incorporate higher resolution areal imagery and lidar point clouds. From the validation data, it is known that the lidar data is not limited by overhanging vegetation. The extracted waterbodies can be incorporated into both the map of overlaid polygons and the temporal shift across the defined cross sections. This increases both temporal resolution by adding more data, as well as leverage the higher spatial resolutions for higher precision extraction. Data fusion was proved to be effective for monitoring by (Joshi et al., 2016; Schmitt & Zhu, 2016).

Also, for waterbody extraction, there are further opportunities with regards to models. As indicated by Y. Li et al (2022), deep learning approaches have a higher average accuracy compared to non-deep learning methods. Therefore, researching these methods have the potential to achieve higher accuracies than have currently been achieved.

5 CONCLUSION

The aim of this research was to determine the most accurate method for waterbody extraction, with the goal to increase temporal resolution of hydromorphological monitoring based on Superview-1 images for shallow streams. The context for this is that most waterbodies do not comply with the KRW, as set by the European union and the Dutch government. Earlier studies substantiated the importance of monitoring the hydromorphology of water steams as it is deemed a crucial process to grasp the ecological status of the stream. A Support Vector Machine model trained on multiple images emerged as the best method for waterbody extraction with a classification accuracy of 90% (Kappa: 0.72). The Otsu threshold method gained an accuracy of 90% (Kappa:0.70), while a Support Vector Machine trained on single images achieved lower accuracy of 76% (Kappa:0.50). Overhanging vegetation was a limitation identified at the beginning of the study however, this study could not resolve this. Also, cloud (shadow) masking are also well-established fields in remote sensing, however these methods were note implemented due to time constraints.

Hydromorphological monitoring based on the extracted waterbodies resulted in a map with the extracted polygons over time. Additionally, a graph indicating the amount of bank and channel shift of the river, measured over a specified cross section was created. The river banks a centre point shifted between 4.5 and 8.6 meters across the four different cross sections during the study period at the eroding section. The centre point of the non-eroding section shifted between 0.2 and 1.3 meters at the end of the study period. The left shifted a maximum of 8.6 meters, whereas the right bank shifted a maximum of 13.1 meters during the study period 2019 – 2023 at the eroding section.

The temporal resolution of this method, with between fifteen to seventeen images, in a period of three years. Hence, the temporal of this study was around five yearly images. Therefore, resolution was significantly increased compared to existing research assessing the change in morphology of a waterbody.

Towards monitoring the ecological status of surface water, this research allowed for high temporal monitoring of the hydromorphological processes. Understanding this process creates valuable context for assessing the full health of a water stream ecosystem. This research serves as context for what the contribution of Superview-1 imagery could be for the monitoring of WFD hydromorphological goals.

Further research should investigate opportunities to increase the accuracy of waterbody extraction. Interpolation methods for overhanging vegetation and probabilistic approach for multi-temporal analysis provide the potential the ability to detect overhanging vegetation. Additionally, data fusion methods could further increase temporal resolution along with leveraging the high spatial accuracy of lidar scans and aerial imagery.

6 REFERENCES

Actueel Hoogtebestand Nederland. (2020). *AHN4 C_69AN2.LAZ*. AHN4. https://geotiles.nl/

Ahmad, S., Kalra, A., & Stephen, H. (2010). Estimating soil moisture using remote sensing data: A machine learning approach. *Advances in Water Resources*, *33*(1), 69–80. https://doi.org/10.1016/j.advwatres.2009.10.008

AHN. (n.d.-a). *Classificatie*. Actueel Hoogtebestand Nederland. Retrieved June 2, 2023, from https://www.ahn.nl/4-classificatie

AHN. (n.d.-b). *Kwaliteitsbeschrijving*. Actueel Hoogtebestand Nederland. Retrieved May 9, 2023, from https://www.ahn.nl/kwaliteitsbeschrijving

AHN. (2020, December 3). *Voortgang AHN 2020 - Externe weergave - Overzicht*. https://www.arcgis.com/home/item.html?id=273cd606b6e04e128f1480e2d4b3a822

Antonarakis, A. S., Richards, K. S., & Brasington, J. (2008). Object-based land cover classification using airborne LiDAR. *Remote Sensing of Environment*, *112*(6), 2988–2998. https://doi.org/10.1016/j.rse.2008.02.004

Basheer, S., Wang, X., Farooque, A. A., Nawaz, R. A., Liu, K., Adekanmbi, T., & Liu, S. (2022). Comparison of Land Use Land Cover Classifiers Using Different Satellite Imagery and Machine Learning Techniques. *Remote Sensing*, *14*(19). https://doi.org/10.3390/rs14194978

Belletti, B., Rinaldi, M., Buijse, A. D., Gurnell, A. M., & Mosselman, E. (2015). A review of assessment methods for river hydromorphology. *Environmental Earth Sciences*, *73*(5), 2079–2100. https://doi.org/10.1007/s12665-014-3558-1

Campbell, J. E., & Shin, M. (2012). *Geographic Information System Basics v. 1.0* (pp. 97–99). lardbucket. http://lardbucket.org

Cheng, Q., Shen, H., Zhang, L., Yuan, Q., & Zeng, C. (2014). Cloud removal for remotely sensed images by similar pixel replacement guided with a spatio-temporal MRF model. *ISPRS Journal of Photogrammetry and Remote Sensing*, *92*, 54–68. https://doi.org/10.1016/j.isprsjprs.2014.02.015

CLO. (2022). *Waterkwaliteit KRW*. https://www.clo.nl/indicatoren/nl1438-kwaliteit-oppervlaktewater-krw

Cohen, J. (1960). A Coefficient of agreement for Nominal Scales. *Educational and Psychological Measurement*, *XX*(1). https://doi.org/https://doi.org/10.1177/001316446002000104

Corenblit, D., Baas, A., Balke, T., Bouma, T., Fromard, F., Garófano-Gómez, V., González, E., Gurnell, A. M., Hortobágyi, B., Julien, F., Kim, D., Lambs, L., Stallins, J. A., Steiger, J., Tabacchi, E., & Walcker, R. (2015). Engineer pioneer plants respond to and affect geomorphic constraints similarly along water-terrestrial interfaces world-wide. *Global Ecology and Biogeography*, *24*(12), 1363–1376. https://doi.org/10.1111/GEB.12373

de Moor, J. J. W. (2007). *Human impact on Holocene catchment development and fluvial processes : the Geul River catchment, SE Netherlands*. s.n.].

de Moor, J. J. W., van Balen, R. T., & Kasse, C. (2007). Simulating meander evolution of the Geul River (the Netherlands) using a topographic steering model. *Earth Surface Processes and Landforms*, *32*(7), 1077–1093. https://doi.org/10.1002/ESP.1466

de Moor, J. J. W., & Verstraeten, G. (2008). Alluvial and colluvial sediment storage in the Geul River catchment (The Netherlands) - Combining field and modelling data to construct a Late Holocene sediment budget. *Geomorphology*, *95*(3–4), 487–503. https://doi.org/10.1016/j.geomorph.2007.07.012

Donchyts, G., Baart, F., Winsemius, H., Gorelick, N., Kwadijk, J., & de Giesen, N. (2017). The Deltares aqua monitor. *Hydrolink*. https://iahr.oss-accelerate.aliyuncs.com/library/HydroLink/HydroLink2017_02_37th_IAHR_Congress.pdf.

Donchyts, G., Baart, F., Winsemius, H., Gorelick, N., Kwadijk, J., & Van De Giesen, N. (2016). Earth's surface water change over the past 30 years. In *Nature Climate Change* (Vol. 6, Issue 9, pp. 810–813). Nature Publishing Group. https://doi.org/10.1038/nclimate3111

Donchyts, G., Schellekens, J., Winsemius, H., Eisemann, E., & van de Giesen, N. (2016). A 30 m resolution surfacewater mask including estimation of positional and thematic differences using landsat 8, SRTM and OPenStreetMap: A case study in the Murray-Darling basin, Australia. *Remote Sensing*, *8*(5). https://doi.org/10.3390/rs8050386

Dong, Y., Fan, L., Zhao, J., Huang, S., Geiß, C., Wang, L., & Taubenböck, H. (2022). Mapping of small water bodies with integrated spatial information for time series images of optical remote sensing. *Journal of Hydrology*, *614*, 128580. https://doi.org/10.1016/J.JHYDROL.2022.128580

Dragićević, S., Pripužić, M., Živković, N., Novković, I., Kostadinov, S., Langović, M., Milojković, B., & Čvorović, Z. (2017). Spatial and temporal variability of bank erosion during the period 1930–2016: Case study—Kolubara River Basin (Serbia). *Water (Switzerland)*, *9*(10). https://doi.org/10.3390/w9100748

EOS-a. (n.d.). *SuperView 1*. Retrieved June 22, 2023, from https://eos.com/find-satellite/superview-1/

EOS-b. (n.d.). *Normalized Difference Water Index*. Retrieved June 22, 2023, from https://eos.com/make-an-analysis/ndwi/

Esri. (n.d.). *2D, 3D & 4D GIS Mapping Software | ArcGIS Pro*. Retrieved May 26, 2023, from https://www.esri.com/en-us/arcgis/products/arcgis-pro/overview

Feizizadeh, B., Darabi, S., Blaschke, T., & Lakes, T. (2022). QADI as a New Method and Alternative to Kappa for Accuracy Assessment of Remote Sensing-Based Image Classification. *Sensors*, *22*(12). https://doi.org/10.3390/s22124506

Gao, B.-C. (1996). NDWI—A normalized difference water index for remote sensing of vegetation liquid water from space. In *REMOTE SENS. ENVIRON* (Vol. 7212). ©Elsevier Science Inc.

González del Tánago, M., Martínez-Fernández, V., Aguiar, F. C., Bertoldi, W., Dufour, S., García de Jalón, D., Garófano-Gómez, V., Mandzukovski, D., & Rodríguez-González, P. M. (2021). Improving river hydromorphological assessment through better integration of riparian vegetation: Scientific evidence and guidelines. *Journal of Environmental Management*, *292*. https://doi.org/10.1016/J.JENVMAN.2021.112730

Helder, D. L., Karki, S., Bhatt, R., Micijevic, E., Aaron, D., & Jasinski, B. (2012). Radiometric calibration of the jandsat MSS sensor series. *IEEE Transactions on Geoscience and Remote Sensing*, *50*(6), 2380–2399. https://doi.org/10.1109/TGRS.2011.2171351

Hemmelder, S., Marra, W., Markies, H., & De Jong, S. M. (2018). Monitoring river morphology & bank erosion using UAV imagery – A case study of the river Buëch, Hautes-Alpes, France. *International Journal of Applied Earth Observation and Geoinformation*, *73*, 428–437. https://doi.org/10.1016/J.JAG.2018.07.016

Higler, L. W. G., & Tolkamp, H. H. (1982). *HYDROPSYCHIDAE AS BIO-INDICATORS**.

Hooke, J. M. (1979). An analysis of the processes of river bank erosion. *Journal of Hydrology*, *42*(1–2), 39–62. https://doi.org/10.1016/0022-1694(79)90005-2

Jiang, W., Ni, Y., Pang, Z., Li, X., Ju, H., He, G., Lv, J., Yang, K., Fu, J., & Qin, X. (2021). An effective water body extraction method with new water index for sentinel-2 imagery. *Water (Switzerland)*, *13*(12). https://doi.org/10.3390/w13121647

Jianya, G., Haigang, S., Guorui, M., & Qiming, Z. (2008). *A REVIEW OF MULTI-TEMPORAL REMOTE SENSING DATA CHANGE DETECTION ALGORITHMS*.

Joshi, N., Baumann, M., Ehammer, A., Fensholt, R., Grogan, K., Hostert, P., Jepsen, M. R., Kuemmerle, T., Meyfroidt, P., Mitchard, E. T. A., Reiche, J., Ryan, C. M., & Waske, B. (2016). A review of the application of optical and radar remote sensing data fusion to land use mapping and monitoring. In *Remote Sensing* (Vol. 8, Issue 1). MDPI AG. https://doi.org/10.3390/rs8010070

Kallis, G., & Butler, D. (2001). The EU water framework directive: measures and implications. *Water Policy*, *3*, 125–142.

Kelcey, J., & Lucieer, A. (2012). Sensor correction of a 6-band multispectral imaging sensor for UAV remote sensing. *Remote Sensing*, *4*(5), 1462–1493. https://doi.org/10.3390/rs4051462

Langat, P. K., Kumar, L., & Koech, R. (2019). Monitoring river channel dynamics using remote sensing and GIS techniques. *Geomorphology*, *325*, 92–102. https://doi.org/10.1016/J.GEOMORPH.2018.10.007

Large, A. R. G., & Gilvear, D. J. (2015). Using Google Earth, A Virtual-Globe Imaging Platform, for Ecosystem Services-Based River Assessment. *River Research and Applications*, *31*(4), 406–421. https://doi.org/10.1002/rra.2798

Leenaers, H. (1989). The dispersal of metal mining wastes in the catchment of the river geul. *Nederlandse Geografische Studies*.

Li, J., Ma, R., Cao, Z., Xue, K., Xiong, J., Hu, M., & Feng, X. (2022). Satellite Detection of Surface Water Extent: A Review of Methodology. In *Water (Switzerland)* (Vol. 14, Issue 7). MDPI. https://doi.org/10.3390/w14071148

Li, Y., Dang, B., Zhang, Y., & Du, Z. (2022). Water body classification from high-resolution optical remote sensing imagery: Achievements and perspectives. In *ISPRS Journal of Photogrammetry and Remote Sensing* (Vol. 187, pp. 306–327). Elsevier B.V. https://doi.org/10.1016/j.isprsjprs.2022.03.013

Liu, Y.-K., Ma, L.-L., Wang, N., Qian, Y.-G., Zhao, Y.-G., Qiu, S., Gao, C.-X., Long, X.-X., & Li, C.-R. (2020). On-orbit radiometric calibration of the optical sensors on-board SuperView-1 satellite using three independent methods. *Optics Express*, *28*(8), 11085. https://doi.org/10.1364/oe.388387

Lu, Y., Wu, P., Ma, X., & Li, X. (2019). Detection and prediction of land use/land cover change using spatiotemporal data fusion and the Cellular Automata–Markov model. *Environmental Monitoring and Assessment*, *191*(2). https://doi.org/10.1007/s10661-019-7200-2

Mercer, B., Glass, N., Allan, J., Rasmussen, J., & Wollersheim, M. (2003). *Orthorectification of Satellite Images using External DEMs from IFSAR AITF-Intermap L-band SAR data project View project ORTHORECTIFICATION OF SATELLITE IMAGES USING EXTERNAL DEMS FROM IFSAR*. https://www.researchgate.net/publication/228770598

Mountrakis, G., Im, J., & Ogole, C. (2011). Support vector machines in remote sensing: A review. In *ISPRS Journal of Photogrammetry and Remote Sensing* (Vol. 66, Issue 3, pp. 247–259). https://doi.org/10.1016/j.isprsjprs.2010.11.001

Mozgovoy, D. K., Hnatushenko, V. V., & Vasyliev, V. V. (2018). AUTOMATED RECOGNITION of VEGETATION and WATER BODIES on the TERRITORY of MEGACITIES in SATELLITE IMAGES of VISIBLE and IR BANDS. *ISPRS Annals of the Photogrammetry, Remote Sensing and Spatial Information Sciences*, *4*(3), 167–172. https://doi.org/10.5194/isprs-annals-IV-3-167-2018

Myneni, R. B., Hall, F. G., Sellers, P. J., & Marshak, A. L. (1995). The Interpretation of Spectral Vegetation Indexes. In *IEEE TRANSACTIONS ON GEOSCIENCE AND REMOTE SENSING* (Vol. 33, Issue 2).

Newson, M. D., Large, A. R. G., Newson, M. D., & Large, A. R. G. (2006). "Natural" rivers, "hydromorphological quality" and river restoration: a challenging new agenda for applied fluvial geomorphology Introduction: Geomorphology Enters River Management. *Earth Surf. Process. Landforms*, *31*, 1606–1624. https://doi.org/10.1002/esp

NSO. (n.d.). *Product levels | Spaceoffice.nl*. Retrieved May 16, 2023, from https://www.spaceoffice.nl/nl/satellietdataportaal/beschikbare-data/uitleg-data/product-levels/

Otsu, N. (1979). A threshold selection mehtod from greay-level Histograms. *IEEE*.

Paul, J. D., Buytaert, W., & Sah, N. (2020). A Technical Evaluation of Lidar-Based Measurement of River Water Levels. *Water Resources Research*, *56*(4). https://doi.org/10.1029/2019WR026810

Pedregosa, F., Michel, V., Grisel, O., Blondel, M., Prettenhofer, P., Weiss, R., Vanderplas, J., Cournapeau, D., Pedregosa, F., Varoquaux, G., Gramfort, A., Thirion, B., Grisel, O., Dubourg, V., Passos, A., Brucher, M., Perrot andÉdouardand, M., Duchesnay, andÉdouard, & Duchesnay EDOUARDDUCHESNAY, Fré. (2011). Scikit-learn: Machine Learning in Python Gaël Varoquaux Bertrand Thirion Vincent Dubourg Alexandre Passos PEDREGOSA, VAROQUAUX, GRAMFORT ET AL. Matthieu Perrot. In *Journal of Machine Learning Research* (Vol. 12). http://scikit-learn.sourceforge.net.

Razaque, A., Ben Haj Frej, M., Almi'ani, M., Alotaibi, M., & Alotaibi, B. (2021). Improved support vector machine enabled radial basis function and linear variants for remote sensing image classification. *Sensors*, *21*(13). https://doi.org/10.3390/s21134431

Rijkswaterstaat. (2021, June 9). *hoogte_grensmaas_2021_laz (69AN2)*. https://downloads.rijkswaterstaatdata.nl/hoogte_2021/hoogte_grensmaas_2021_laz/

Rijkswaterstaat. (2022a, June 5). *Dataregister Rijkswaterstaat*.
https://maps.rijkswaterstaat.nl/dataregister/srv/dut/catalog.search#/metadata/ef8e4034-fe34-42b9-b7b9-14022f2a5415?tab=relations

Rijkswaterstaat. (2022b, June 6). *hoogte_grensmaas_2022_laz (69AN2)*.
https://downloads.rijkswaterstaatdata.nl/hoogte_2022/hoogte_grensmaas_2022_laz/

Rijkswaterstaat. (2023). *Waterinfo*. https://waterinfo.rws.nl/#!/kaart/waterhoogte/

Rocklin, M. (2015). Dask: Parallel Computation with Blocked algorithms and Task Scheduling. In *PROC. OF THE 14th PYTHON IN SCIENCE CONF*. https://www.youtube.com/watch?v=1kkFZ4P-XHg

Rusnák, M., & Lehotské, M. (2014). Time-focused investigation of river channel morphological changes due to extreme floods. *Zeitschrift Fur Geomorphologie*, *58*(2), 251–266. https://doi.org/10.1127/0372-8854/2013/0124

Saylam, K., Brown, R. A., & Hupp, J. R. (2017). Assessment of depth and turbidity with airborne Lidar bathymetry and multiband satellite imagery in shallow water bodies of the Alaskan North Slope. *International Journal of Applied Earth Observation and Geoinformation*, *58*, 191–200. https://doi.org/10.1016/j.jag.2017.02.012

Schmitt, M., & Zhu, X. X. (2016). Data Fusion and Remote Sensing: An ever-growing relationship. *IEEE Geoscience and Remote Sensing Magazine*, *4*(4), 6–23. https://doi.org/10.1109/MGRS.2016.2561021

Shahtahmassebi, A., Yang, N., Wang, K., Moore, N., & Shen, Z. (2013). Review of shadow detection and de-shadowing methods in remote sensing. In *Chinese Geographical Science* (Vol. 23, Issue 4, pp. 403–420). https://doi.org/10.1007/s11769-013-0613-x

sklearn. (2023). *sklearn.metrics.cohen_kappa_score*. https://scikit-learn.org/stable/modules/generated/sklearn.metrics.cohen_kappa_score.html

SpaceWill. (n.d.). *Key parameters for SV-2*. Retrieved May 22, 2023, from https://www.spaceoffice.nl/nl/satellietdataportaal/specificatie-data/superview-1-en--2/

STOWA. (2020). *Referenties en maatlatten voor natuurlijke watertypen voor de Kaderrichtlijn Water 2021-2027, versie juni 2020*.
https://www.stowa.nl/sites/default/files/assets/PUBLICATIES/Publicaties%202018/STOWA%202018-49%20Maatlatten%20-%202020v4.pdf

Stutter, M., Baggaley, N., Ó hUallacháin, D., & Wang, C. (2021). The utility of spatial data to delineate river riparian functions and management zones: A review. *Science of the Total Environment*, *757*. https://doi.org/10.1016/J.SCITOTENV.2020.143982

Talukdar, S., Singha, P., Mahato, S., Shahfahad, Pal, S., Liou, Y. A., & Rahman, A. (2020). Land-use land-cover classification by machine learning classifiers for satellite observations-A review. In *Remote Sensing* (Vol. 12, Issue 7). MDPI AG. https://doi.org/10.3390/rs12071135

Thanh Noi, P., & Kappas, M. (2017). Comparison of Random Forest, k-Nearest Neighbor, and Support Vector Machine Classifiers for Land Cover Classification Using Sentinel-2 Imagery. *Sensors (Basel, Switzerland)*, *18*(1). https://doi.org/10.3390/s18010018

van Heeringen, K.-J., Asselman, N., Overeem, A., Beersma, J., & Philip, S. (2022). *Analyse overstroming Valkenburg*.

van Leeuwen, B., Tobak, Z., & Kovács, F. (2020). Sentinel-1 and-2 based near real time inland excess water mapping for optimized water management. *Sustainability (Switzerland)*, *12*(7). https://doi.org/10.3390/su12072854

Vogel, R. M., & Asce, M. (2011). Hydromorphology. *Journal of Water Resources Planning and Management*, *137*(2), 147–149. https://doi.org/10.1061/(ASCE)WR.1943-5452.0000122

Vos, K., Splinter, K. D., Harley, M. D., Simmons, J. A., & Turner, I. L. (2019). CoastSat: A Google Earth Engine-enabled Python toolkit to extract shorelines from publicly available satellite imagery. *Environmental Modelling and Software*, *122*. https://doi.org/10.1016/J.ENVSOFT.2019.104528

Warrens, M. J. (2015). Five Ways to Look at Cohen's Kappa. *Journal of Psychology & Psychotherapy*, *05*(04). https://doi.org/10.4172/2161-0487.1000197

Winterbottom, S. J., & Gilvear, D. J. (2000). A GIS-based approach to mapping probabilities of river bank erosion: Regulated river tummel, Scotland. *River Research and Applications*, *16*(2), 127–140. https://doi.org/10.1002/(sici)1099-1646(200003/04)16:2<127::aid-rrr573>3.0.co;2-q

Woodget, A. S., Austrums, R., Maddock, I. P., & Habit, E. (2017). Drones and digital photogrammetry: from classifications to continuums for monitoring river habitat and hydromorphology. *Wiley Interdisciplinary Reviews: Water*, *4*(4). https://doi.org/10.1002/WAT2.1222

Xie, G., Wang, M., Zhang, Z., Xiang, S., & He, L. (2021). Near real-time automatic sub-pixel registration of panchromatic and multispectral images for pan-sharpening. *Remote Sensing*, *13*(18). https://doi.org/10.3390/rs13183674

Xu, H. (2006). Modification of normalised difference water index (NDWI) to enhance open water features in remotely sensed imagery. *International Journal of Remote Sensing*, *27*(14), 3025–3033. https://doi.org/10.1080/01431160600589179

Yan, W. Y., Shaker, A., & El-Ashmawy, N. (2015). Urban land cover classification using airborne LiDAR data: A review. In *Remote Sensing of Environment* (Vol. 158, pp. 295–310). Elsevier Inc. https://doi.org/10.1016/j.rse.2014.11.001

Zeng, C., Bird, S., Luce, J. J., & Wang, J. (2015). A natural-rule-based-connection (NRBC) method for river network extraction from high-resolution imagery. *Remote Sensing*, *7*(10), 14055–14078. https://doi.org/10.3390/rs71014055

Zewdie, W., & Csaplovics, E. (2015). Remote sensing based multi-temporal land cover classification and change detection in northwestern ethiopia. *European Journal of Remote Sensing*, *48*, 121–139. https://doi.org/10.5721/EuJRS20154808

APPENDIX

I. PREDICTION IMAGES

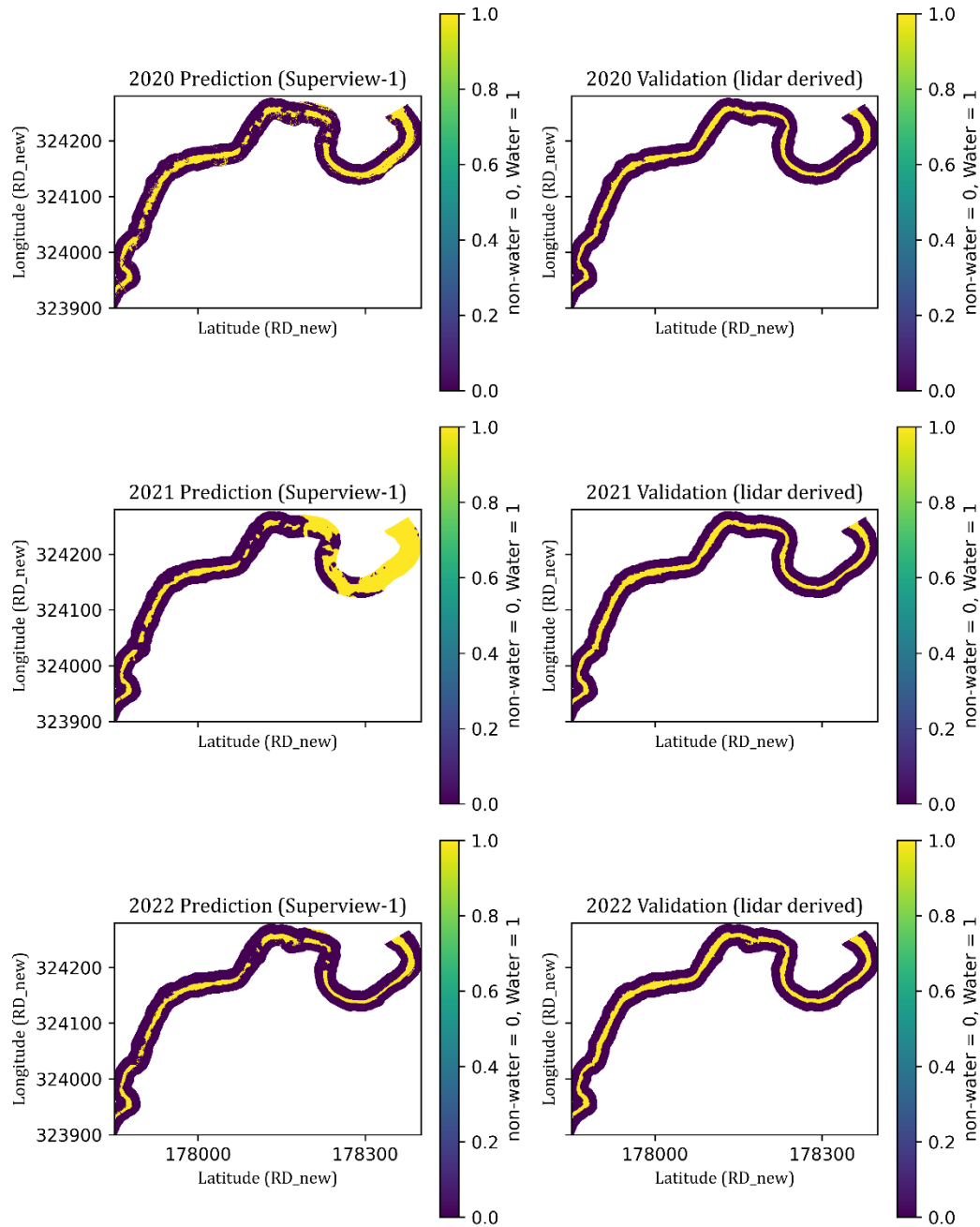### OTSU THRESHOLD METHOD (ERODING SECTION)

Fig.11. *Prediction and validation of Otsu threshold method (Eroding section)*
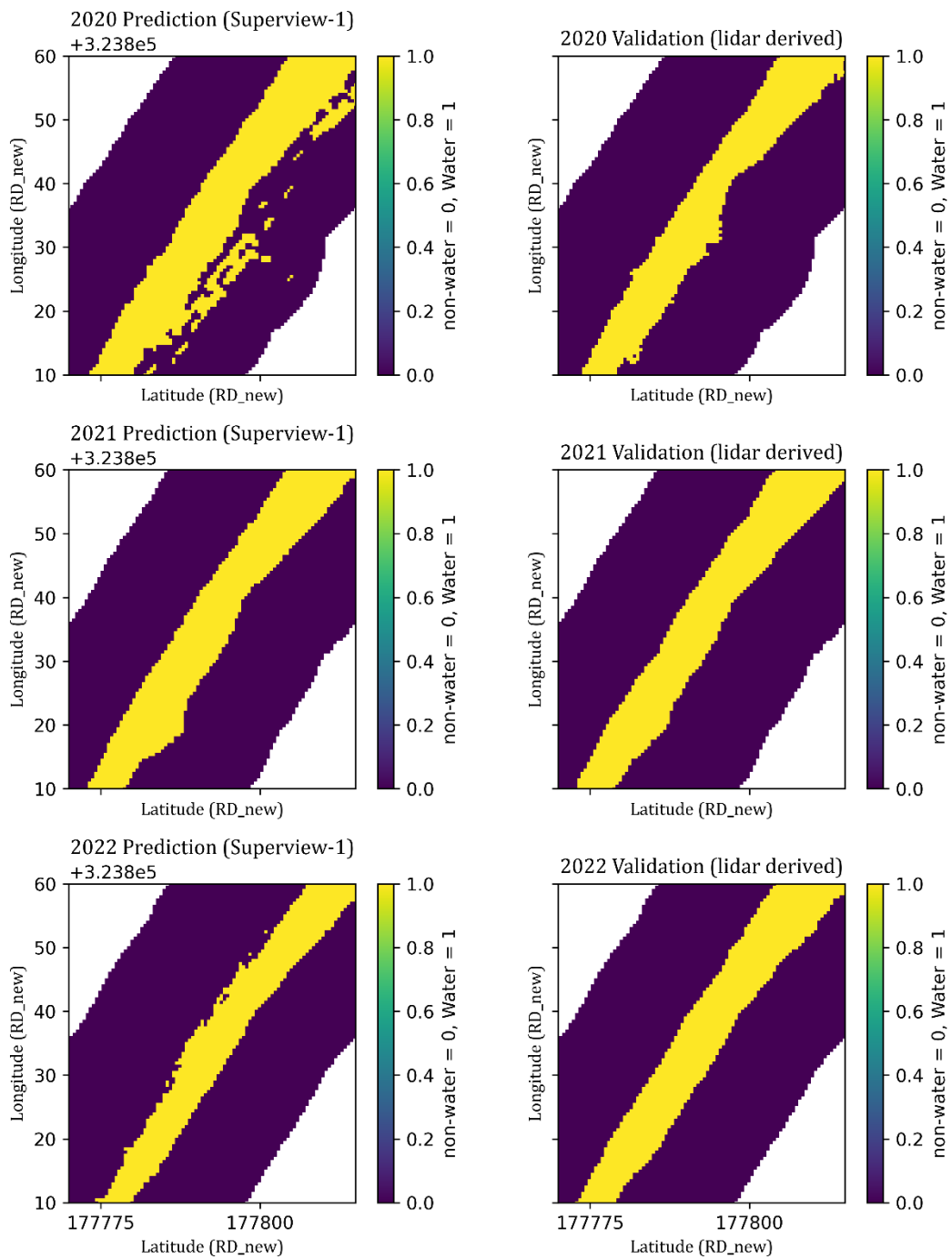
OTSU THRESHOLD METHOD (NON-ERODING SECTION)

Fig.12. *Prediction and validation of Otsu threshold method (non-eroding section)*
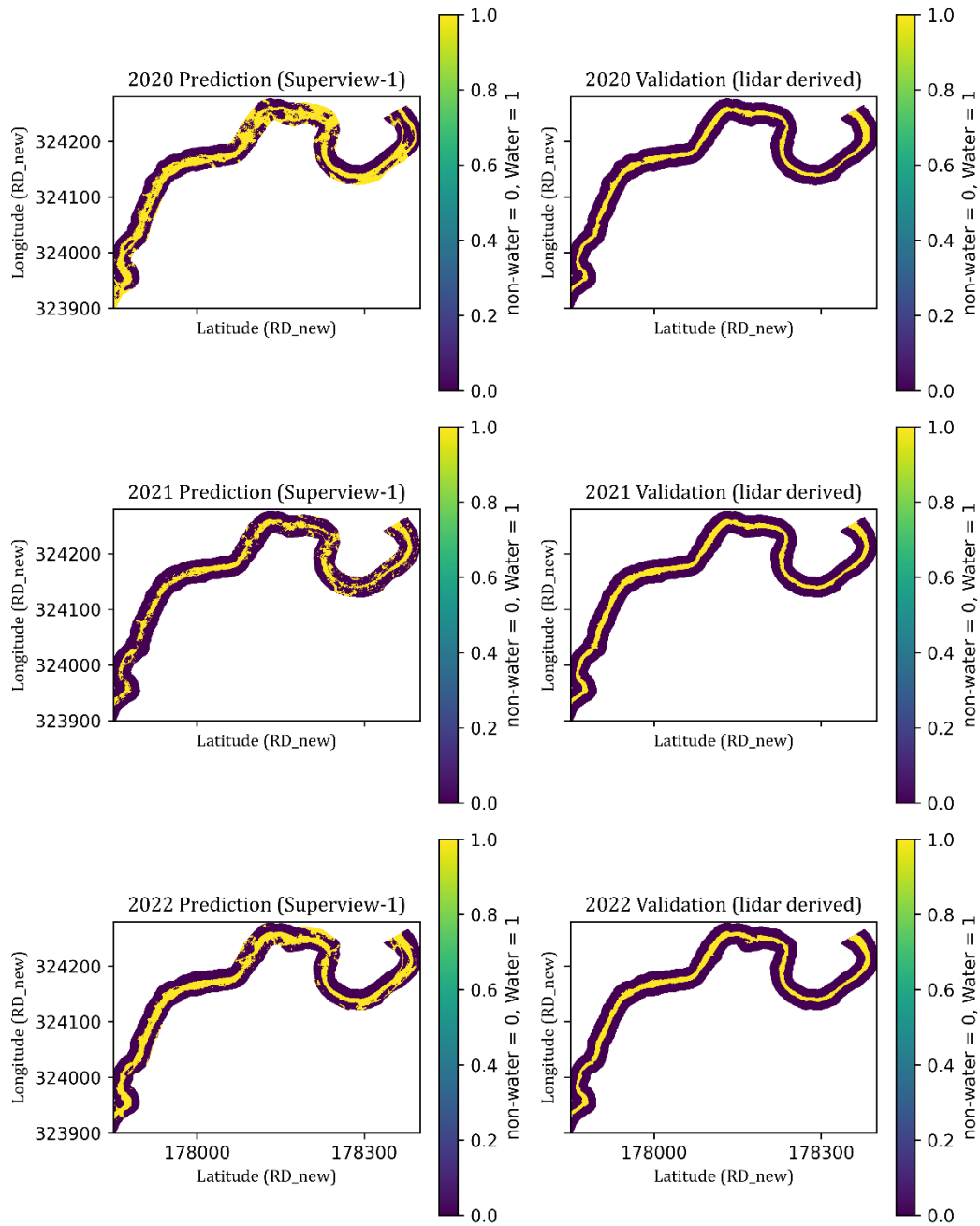
SINGLE IMAGE ML METHOD (ERODING SECTION)

Fig.13. *Prediction and validation of Singe image ML method (eroding section)*

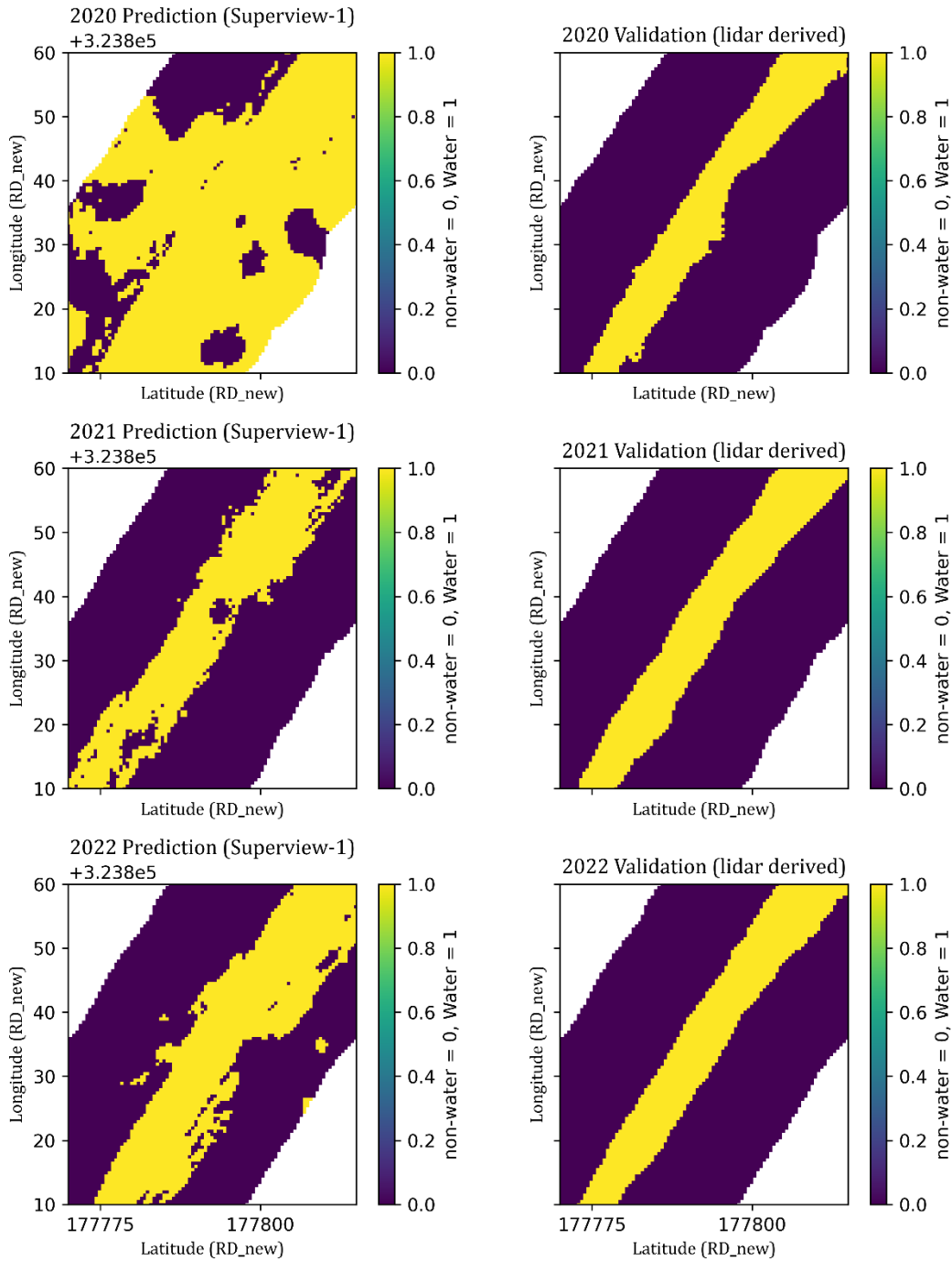# SINGLE IMAGE ML METHOD (NON-ERODING SECTION)

Fig.14. *Prediction and validation of Singe image ML method (non-eroding section)*

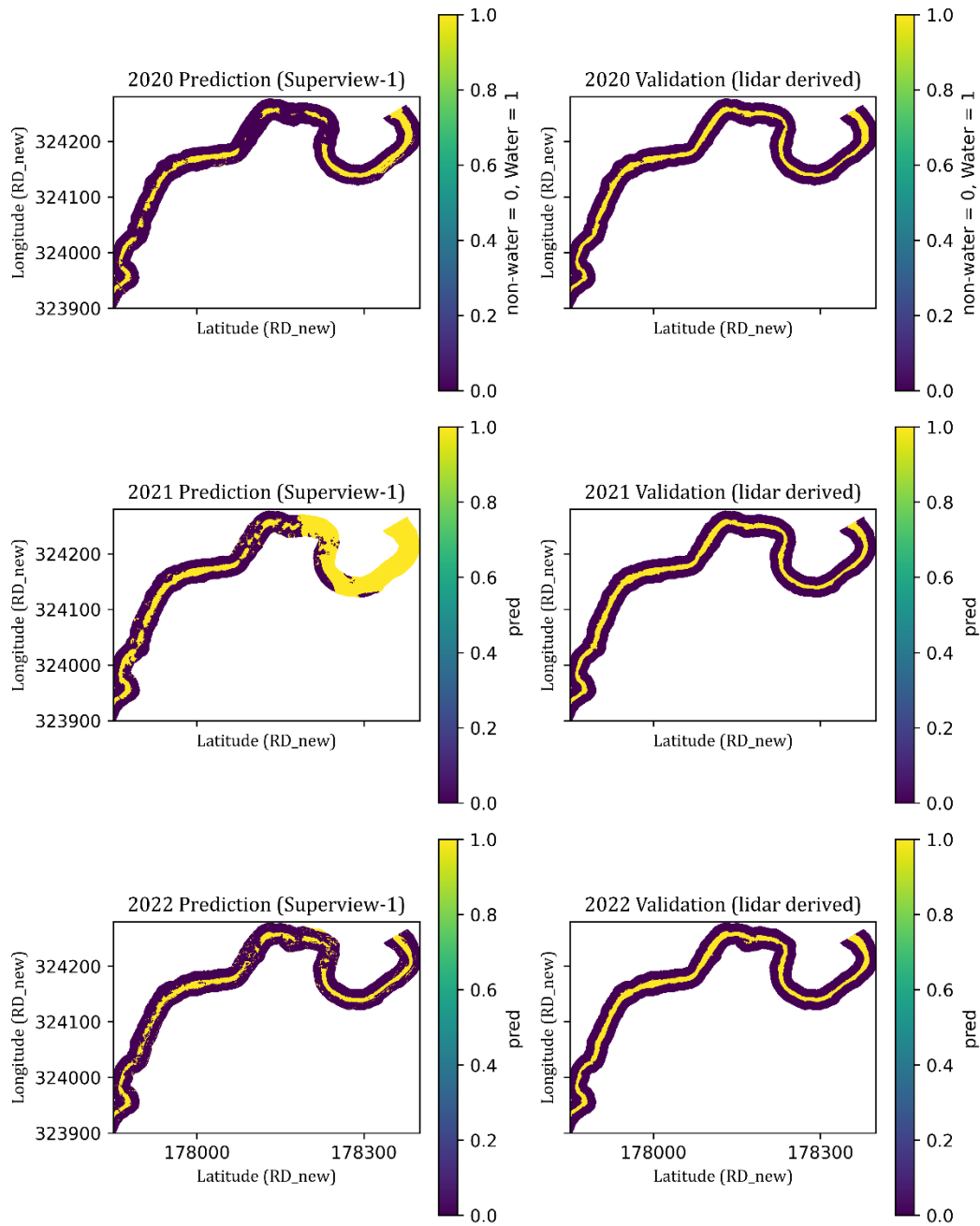# MULTI IMAGE ML METHOD (ERODING SECTION)

Fig.15. *Prediction and validation of Multi image ML method (eroding section)*

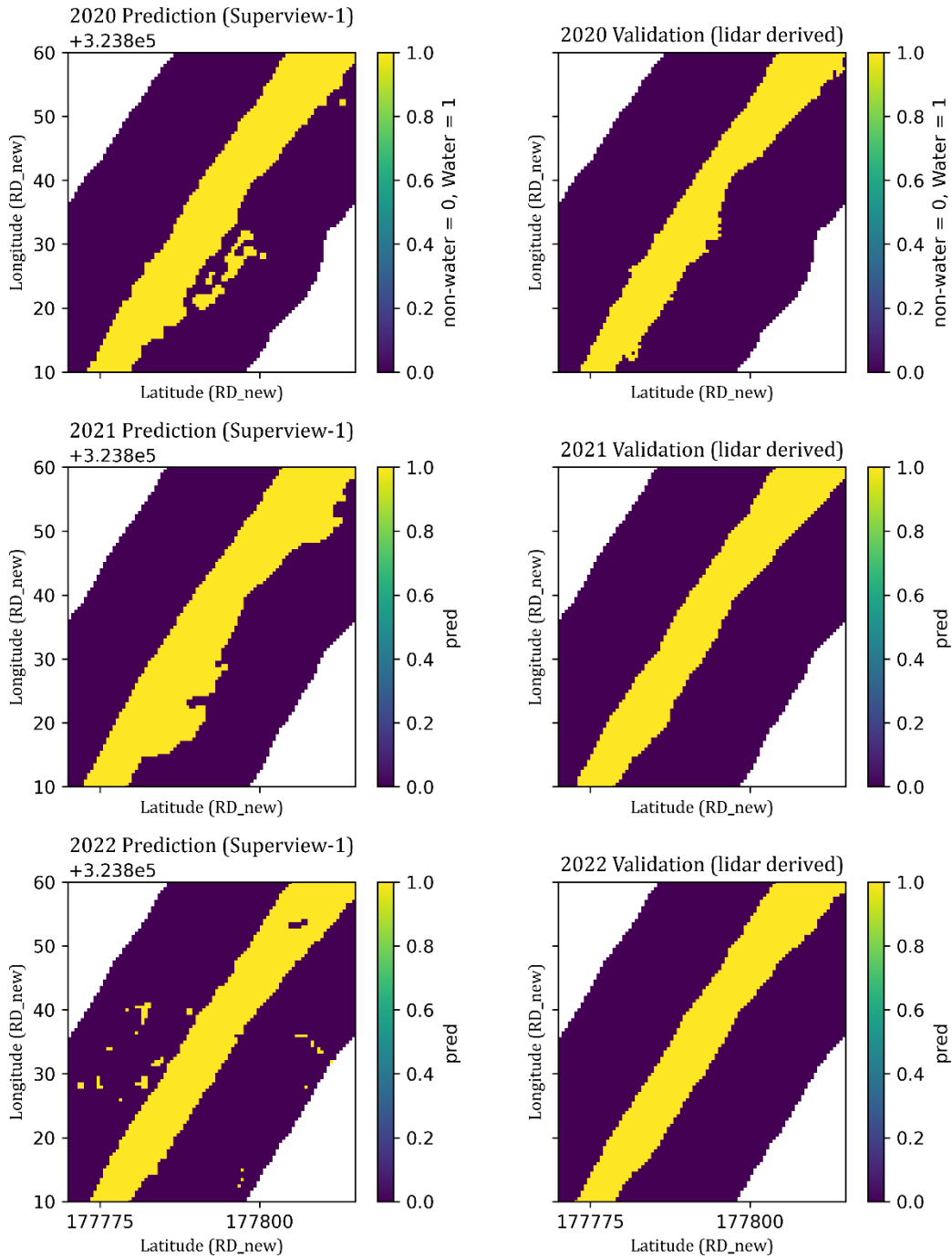## MULTI IMAGE ML METHOD (NON-ERODING SECTION)

Fig.16. *Prediction and validation of Multi image ML method (non-eroding section)*